

PROTOPLANETARY DISK WINDS BY MAGNETOROTATIONAL INSTABILITY : FORMATION OF AN INNER HOLE AND A CRUCIAL ASSIST FOR PLANET FORMATION

TAKERU K. SUZUKI^{1,2}, TAKAYUKI MUTO³ & SHU-ICHIRO INUTSUKA^{1,3}

Draft version November 13, 2018

ABSTRACT

By constructing a global model based on 3D local magnetohydrodynamical (MHD) simulations, we show that the disk wind driven by magnetorotational instability (MRI) plays a significant role in the dispersal of the gas component of proto-planetary disks. Because the mass loss time scale by the MRI-driven disk winds is proportional to the local Keplerian rotation period, a gas disk dynamically evaporates from the inner region with possibly creating a gradually expanding inner hole, while a sizable amount of the gas remains in the outer region. The disk wind is highly time-dependent with quasi-periodicity of several times Keplerian rotation period at each radius, which will be observed as time-variability of protostar-protoplanetary disk systems. These features persistently hold even if a dead zone exists because the disk winds are driven from the surface regions where ionizing cosmic rays and high energy photons can penetrate. Moreover, the predicted inside-out clearing significantly suppresses the infall of boulders to a central star and the Type I migration of proto-planets which are favorable for the formation and survival of planets.

Subject headings: accretion, accretion disks — MHD — stars: winds, outflows — planetary systems: formation — planetary systems: protoplanetary disks — turbulence

1. INTRODUCTION

Planets are believed to form in protoplanetary disks consisting of gas and dust components around newly born stars. The evolution of the gas component is crucial in determining the final state of the planetary system, such as the number and locations of terrestrial (rocky) and Jovian (gas-giant) planets (Ida & Lin 2004). The amount of the gas that is captured by Jovian planets is generally much smaller than the total gas of the disk. Therefore, the gas component should dissipate via other mechanisms with the observationally inferred timescale of $10^6 - 10^7$ yr (e.g., Haisch, Lada, & Lada 2001; Hernández et al. 2008). The currently favored scenario is that the gas dissipates by the combination of photoevaporation by Ultraviolet (UV) flux from a central star and viscous accretion (e.g. Shu, Johnstone, & Hollenback 1992; Matsuyama, Johnstone, & Hartmann 2003; Takeuchi, Clarke, & Lin 2005; Alexander, Clarke, & Pringle 2006; Chiang & Murray-Clay 2007). However, the time-evolution of the luminosity and spectrum of the UV radiation is quite uncertain, and moreover some observed transitional disks with inner holes are inconsistent with the photoevaporation mechanism (Calvet et al. 2005; Espaillat et al. 2008; Hughes et al. 2009).

By performing local 3D ideal MHD simulations in the shearing box approximation (Hawley, Gammie, & Balbus 1995; Matsumoto & Tajima 1995), Suzuki & Inutsuka (2009, SI09 hereafter) have shown that MHD turbulence in protoplanetary disks effectively drives disk winds. The local timescale of the dynamical evaporation by magnetorotational instability (MRI) driven disk

winds is defined as

$$\tau_{\text{ev}} = \Sigma / (\rho v_z)_w, \quad (1)$$

where $(\rho v_z)_w$ is the sum of the mass fluxes from the upper and lower disk surfaces and Σ is the surface density. We can estimate $\tau_{\text{ev}} \sim$ several thousand years at 1 AU of the typical protosolar disk (e.g., minimum mass solar nebula, or MMSN in short hereafter; Hayashi 1981); here we use the typical values, $\Sigma = 1700 \text{ g cm}^{-2}$ and $(\rho v_z)_w \sim 10^{-8} \text{ g cm}^{-2} \text{ s}^{-1}$ (see §2.2 for the scaling of the disk wind flux). While the actual dispersal time is much longer as shown in this paper because the radial mass accretion is not taken into account here, this estimate shows that the MRI-driven disk wind should play a significant role in the dispersal of protoplanetary disks. In this paper, we investigate the evolution of gas density with disk winds and radial mass accretion in a global model.

In SI09, we did not take into account the effects of a so-called dead zone which is inactive with respect to MRI because of the insufficient ionization for the coupling between gas and magnetic fields. The dead zone is believed to form around the midplane in the inner parts of protoplanetary disks because ionizing cosmic rays and X-rays cannot penetrate from the disk surfaces (Sano et al. 2000). In this paper, we improve the models of SI09 by investigating the effects of dead zones by performing resistive MHD simulations.

The construction of the paper is as follows : We firstly describe the MHD simulations in local shearing boxes with and without dead zones in §2. In §3 we describe our global model. In §4, we show how the MRI disk winds disperse the gas component of protoplanetary disks from the inner part. Also, we show its effects on the planet formation. In §5, we discuss the properties of disk evolution mainly focusing on the escape of the disk winds from the gravity of a central star.

2. LOCAL SIMULATIONS

stakeru@nagoya-u.jp

¹ Department of Physics, Nagoya University, Nagoya, Aichi 464-8602, Japan

² School of Arts and Sciences, University of Tokyo, Komaba, Meguro, Tokyo, Japan, 153-8902

³ Department of Physics, Kyoto University, Kyoto, Japan, 606-8502

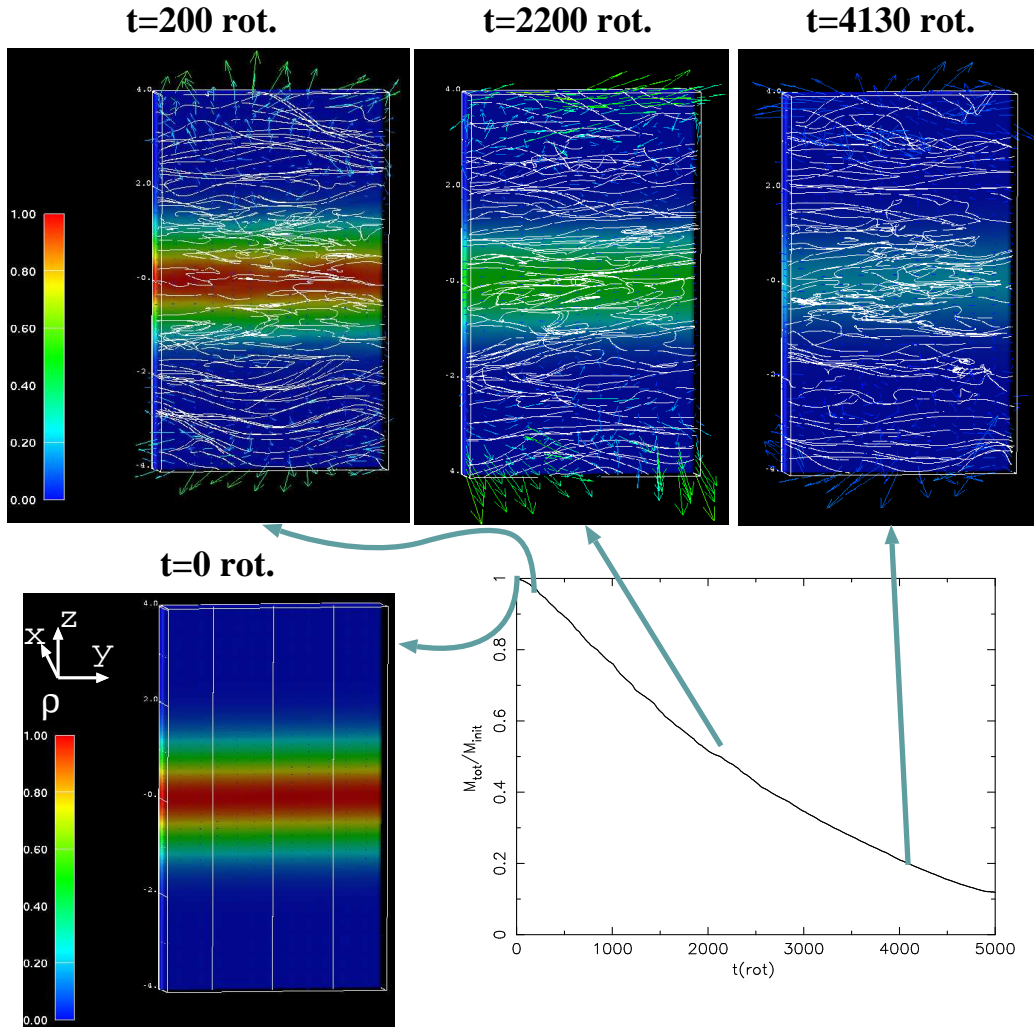


FIG. 1.— Dynamical evaporation of a protoplanetary gas disk by local 3D ideal MHD simulation without mass supply by radial accretion. We impose weak vertical magnetic field, B_z , with the plasma β value, $\beta_{z,\text{mid}} = 8\pi\rho_{\text{mid}}c_s^2/B_z^2 = 10^6$, at the midplane. The lower right panel shows the total mass normalized by the initial mass in the local simulation box as a function of rotation time. The four color panels show the snapshots of the local protoplanetary disk simulation at $t = 0$ (initial condition), 200 rotations, 2200 rotations, and 4130 rotations. The x , y , and z components respectively correspond to radial, azimuthal, and vertical components. The unit of each component is scale height, $H \equiv \sqrt{2}c_s/\Omega$. The box size is $(x, y, z) = (\pm 0.5H, \pm 2H, \pm 4H)$, which is resolved by $(32, 64, 256)$ grid points. The colors indicate density normalized by the initial value at the midplane, the white solid lines illustrate magnetic field lines, and the arrows show velocity field. A small number of magnetic field lines (vertical lines) in the panel of $t = 0$ reflect that the initially imposed magnetic field is weak (the number of field lines is scaled by magnetic field strength). We should emphasize that the actual dispersal is much slower because of the mass supply by accretion (see text).

The main purpose of this section is to determine the turbulent viscosity and the mass flux of the disk winds which are used in the global models in §3. For that purpose, we perform 3D MHD simulations of a local protoplanetary (accretion) disk in the shearing box coordinate (Hawley, Gammie, & Balbus 1995). We use the simulation box with $(x, y, z) = (\pm 0.5H, \pm 2H, \pm 4H)$, where the x , y , and z components respectively correspond to radial, azimuthal, and vertical components and scale height, H , is defined from sound speed, c_s , and disk rotation frequency, Ω , as $H \equiv \sqrt{2}c_s/\Omega$.

In SI09 we have already shown results of ideal MHD simulation in the shearing box up to 400 rotation time. In this paper, we first extend this simulation until 5000 rotation time when the significant mass is lost from the simulation box (§2.2). In §2.3 we take into account the

effects of resistivity (*i.e.* dead zone). Later in this paper, we perform simulations in boxes with larger vertical extents to study the effects of the box size on the escaping mass (§5.4.1).

2.1. Launching of Disk Winds

Before showing results of the local simulations, we discuss basic properties of the disk wind obtained in SI09 because the disk wind is a key that controls the evolution of protoplanetary disks in this paper. In SI09 we interpreted that the disk winds are driven by the breakups of channel-mode flows (e.g. Sano et al. 2004) as a result of MRI (Balbus & Hawley 1991). Large-scale channel flows (e.g. Sano et al. 2004) develop most effectively at 1.5 - 2 times the scale height above the midplane. The breakups of these channel flows by magnetic reconnections drive disk winds in a time-dependent

manner with quasi-periodic cycles of 5-10 rotation period. The disk material itself is lift up recurrently, which will be observed as the time variation of effective disk surfaces. Time-variabilities are actually observed in protostar-protoplanetary disk systems (e.g. Wisniewski et al. 2009; Muzerolle et al. 2009; Bary, Leisenring, & Skruskie 2009), which might be explained by quasi-periodic breakups of channel flows. The quasi-periodic feature of the disk winds is universally found not only in ideal MHD simulations but in simulations with dead zones as will be shown in §2.3.

We should note that upward motions in vertically stratified accretion disks have been widely discussed with various interpretations. Magnetic buoyancy (Parker instability; Parker 1966) is one of the mechanism in uplifting mass and magnetic field in the upper regions with $|z| \gtrsim 1.5H$ (Miller & Stone 2000; Machida, Hayashi, & Matsumoto 2000; Nishikori, Machida, & Matsumoto 2006). In fact, we observe \sim -shape magnetic field structures, which are characteristic of Parker instability, in our simulations as well (Figure 1). Recently, Latter, Fromang, & Gressel (2010) also discussed that channel flows are moving upward by magnetic buoyancy in a stratified disk. Magnetic buoyancy may play a role in upward flows and magnetic fields in cooperating with MRI channel flows in the upper regions ($|z| \gtrsim 1.5H$). Detailed analysis of the role of magnetic buoyancy is driving the disk winds remains to be done.

Flows and magnetic motions around the midplane show complicated behaviors. On one hand, magnetic pattern seems to propagate away from the midplane (Davis, Stone, & Pessah 2010; Gressel 2010, ; our simulation shows the same trend.). Since this region is buoyantly stable (Shi, Krolik, & Hirose 2010), this apparent propagating pattern may be due to a different mechanism from magnetic buoyancy. Brandenburg et al. (1995, see also Gressel 2010) try to interpret this upgoing pattern from dynamo waves (Parker 1955; Yoshimura 1975; Vishniac & Brandenburg 1997). On the other hand, the direction of the Poynting flux associated with magnetic tension is toward the midplane as we have shown in SI09. We explained that the breakups of large-scale channel flows at injection regions, $z \approx \pm 1.5H$, drive mass motions to a midplane as well as surfaces.

Although properties of vertical flows and magnetic motions are not clearly understood in detail, upward flows in $z \gtrsim$ a few scale heights seem to be robust phenomena in stratified disks. The mass loading at the injection regions appear to be operated by the breakups of channel flows of MRI, and magnetic buoyancy also plays a role in lifting up the gas in the upper regions.

2.2. Disks without Dead Zone

We show results of the ideal MHD simulations in this subsection. We adopt the same resolution of the grid points, $(x, y, z) = (32, 64, 256)$, as in SI09 for runs with different net vertical magnetic flux. In addition to the standard resolution runs, we perform the simulations with higher resolution, $(x, y, z) = (64, 128, 512)$, in some cases. Extending from SI09, we carry out a long-time simulation in this paper until the significant mass is lost from the local box by the disk wind. Figure 1 is the result of the initial plasma β value, $\beta_{z,\text{mid}} = 8\pi\rho_{\text{mid}}c_s^2/B_z^2 =$

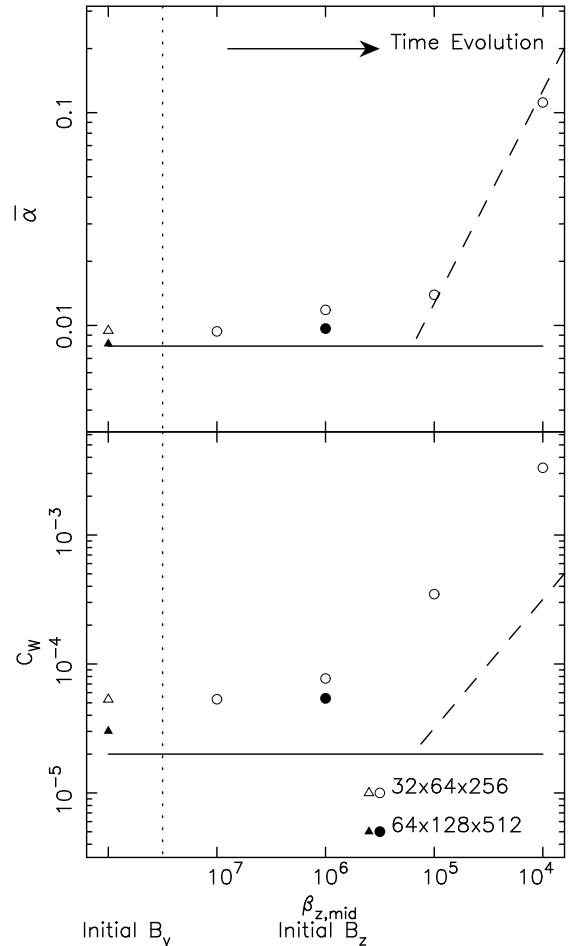


FIG. 2.— Dependences of averaged turbulent viscosity, $\bar{\alpha}$, (top) and mass flux of disk winds, C_w , (bottom) on the initial plasma $\beta_{z,\text{mid}} (= 8\pi\rho_{\text{mid}}c_s^2/B_z^2)$ values for the net vertical field, B_z . The left-most grid corresponds to the initial toroidal field cases. The open symbols are the results of the standard resolution simulations with mesh points $(x, y, z) = (32, 64, 256)$ and the filled symbols are the results of the higher resolution of $(64, 128, 512)$. The solid lines represent $\bar{\alpha}_{\text{fl}}$ and $C_{w,\text{fl}}$, which we use for the global model. The dashed lines denote the linear dependence on $\beta_{z,\text{mid}}^{-1}$.

10^6 , at the midplane for net vertical magnetic field⁴, B_z , where ρ_{mid} is the density at the midplane. The figure shows that about 90% of the initial gas is dispersed in 5000 rotations (5000 years at 1 AU) if there is no mass supply by accretion. This result shows that the evaporation timescale using Equation (1) gives a reasonable estimate and the MRI-driven disk winds should significantly affect the evolution of protoplanetary disks.

From the results of the local MHD simulations, we can determine the Shakura & Sunyaev (1973) α viscosity and the mass flux of the disk winds. α is calculated from

⁴ Note that the integrated vertical magnetic flux, $\int dx dy B_z$ is a strictly conserved quantity in the local shearing box simulations (Hawley, Gammie, & Balbus 1995), though the magnetic energy of z component $\int dx dy B_z^2/4\pi$ does not conserve. Then, $\beta_{z,\text{mid}}$ is a good indicator of magnetic field strength not only at the initial state but at later times when the magnetic field is amplified by MRI.

anisotropic stress of MHD turbulence,

$$\alpha = (v_x \delta v_y - \frac{B_x B_y}{4\pi\rho})/c_s^2, \quad (2)$$

where $\delta v_y \equiv v_y + (3/2)\Omega x$ is the velocity shift from the background Kepler rotation $(3/2)\Omega x$. We use the average α in the entire simulation box,

$$\bar{\alpha} = \frac{\int \rho \alpha dx dy dz}{\int \rho dx dy dz}. \quad (3)$$

Note that the density weighted average, $\bar{\alpha}$, is directly related to mass accretion rate (e.g., Pringle 1981). As for the disk wind mass flux, we use the nondimensionalized mass flux,

$$C_w = (\rho v_z)_w / (\rho_{\text{mid}} c_s). \quad (4)$$

Figure 2 shows $\bar{\alpha}$ and C_w as functions of $\beta_{z,\text{mid}}$. Note that the net B_z becomes strong from left to right. The left-most grid is for the cases of no net B_z field. In these cases we initially give purely toroidal field, B_y , with the β values of 10^6 in $-3H < z < 3H$, whereas the results do not depend on the initial strength because magnetic flux of y (as well as x) component does not conserve.

The figure exhibits that both $\bar{\alpha}$ and C_w have the floor values for sufficiently weak net vertical magnetic field, $\beta_{z,\text{mid}} \gtrsim 10^6$. In these cases the saturated magnetic field at the midplane gives $\beta (= 8\pi p/B^2) \sim 100$, indicating $\approx 1\%$ of the gas energy is transferred to the magnetic fields (SI09). The saturation level roughly corresponds to the floor value of $\alpha \sim 0.01$ (α is roughly $1/\beta$). Such weak net vertical field gives little effects, because it is much smaller than the turbulent component of the vertical fields. The turbulent component of B_z gives $\langle B_z^2 \rangle / 8\pi \sim 10^{-4} - 10^{-3} p$ even in the zero net vertical field case, where $\langle \rangle$ denotes time-average. This value seems to be determined as the level that is one or two orders of magnitude smaller than the dominant toroidal component ($\langle B_y^2 \rangle / 8\pi \sim p/\beta \sim 0.01 p$). If the net vertical field is much smaller than the turbulent vertical component, $\langle B_z^2 \rangle / 8\pi \leq 10^{-6} p$ the values of α and C_w are not affected by the net vertical field.

On the other hand, for larger magnetic field cases, $\beta_{z,\text{mid}} \lesssim 10^5$, the net vertical magnetic field plays a role, because it is not negligible compared to the turbulent component. $\bar{\alpha}$ and C_w increase almost linearly with magnetic energy of net vertical field ($\propto 1/\beta_{z,\text{mid}}$). The behaviors of $\bar{\alpha}$ and C_w are similar, which indicates that the mass flux of the disk winds is positively correlated with the mass accretion rate. This is reasonable because the energy source of the disk winds is the gravitational energy liberated by accretion, which is discussed in §5.

In the higher resolution runs, the saturation levels of the magnetic fields are slightly lower than the corresponding cases with lower resolutions. Then, both $\bar{\alpha}$ and C_w become slightly smaller in the higher resolution runs. The dependence of the saturation level of magnetic field and α on resolutions is still under debate and widely discussed in various authors (e.g. Balbus & Hawley 1998; Pessah, Chan, & Psaltis 2007)

2.3. Disks with Dead Zone

The temperature of protoplanetary disks are too low to ionize the gas by thermal collisions. Various ionization

sources, such as X-rays, cosmic rays, and radioactive nuclei, have been widely discussed (Umeyayashi & Nakano 1980; Hayashi 1981; Glassgold, Najita, & Igea 1997). The ionization degree at midplanes is generally smaller than that in upper regions because the recombination rate is higher there as a result of higher density. Under certain circumstances, dead zones, in which the gas is decoupled with the magnetic fields due to the insufficient ionization, are supposed to form near midplanes. However, Inutsuka & Sano (2005) also introduced a self-sustained mechanism by current-carrying electrons in turbulent disks, which increases the resultant ionization degree. Thus, calculating ionization degree is not straightforward. In this paper, we study extreme cases which give distinct dead zones. As will be described below, we take into account the ionization by cosmic rays and X-rays. Since they come from disk surfaces, dead zones tend to form near the midplane if the surface density is sufficiently high. We adopt a simple treatment in determining ionization degree and study effects of dead zones on disk winds.

2.3.1. Set-up

To treat dead zones, we take into account resistivity in the induction equation that describes the evolution of magnetic fields :

$$\frac{\partial \mathbf{B}}{\partial t} = \nabla \times (\mathbf{v} \times \mathbf{B} - \eta \nabla \times \mathbf{B}), \quad (5)$$

where η is resistivity which is determined by ionization degree, x_e as $\eta = 234\sqrt{T}/x_e$ (Blaes & Balbus 1994), because electrons control the coupling between gas and magnetic field in high density medium. We assume the temperature structure of the MMSN (Hayashi 1981) :

$$T = 293\text{K} \left(\frac{r}{1 \text{ AU}} \right)^{-1/2}, \quad (6)$$

which can be transformed into the sound speed, $c_s = 0.99\text{km/s} \left(\frac{r}{1 \text{ AU}} \right)^{-1/4}$.

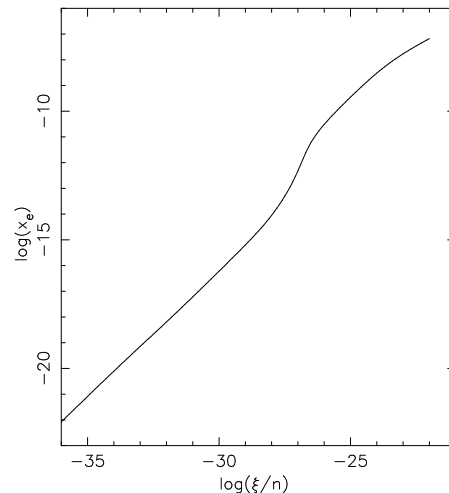


FIG. 3.— Ionization degree, x_e , on ionization rate per number density, ξ/n . The data are taken from Inutsuka & Sano (2005); Sano et al. (2000).

The ionization degree is determined by the balance between ionization and recombination. In this paper, we use the result of previous calculation by Sano et al. (2000) and Inutsuka & Sano (2005), which give x_e as a function of ionization rate, ξ , and local number density, n , by calculating recombination on dust grains and radiative and dissociative recombination in gas phase (see also, e.g. Umebayashi & Nakano 1980; Ilgner & Nelson 2006). When one fixes the abundance of gas and the properties of dust grains, the ionization degree is a function of the only one parameter, ξ/n (Inutsuka & Sano 2005). This is because the recombination is essentially two-body reaction and recombination rate per volume is proportional to n^2 while the ionization rate per volume is ξn . Figure 3 presents x_e for the solar abundance gas with gas-to-dust ratio of 100 and dust grain size of $0.1\mu\text{m}$ (Inutsuka & Sano 2005; Sano et al. 2000). We use this data for our local resistive MHD simulations. We adopt the mean molecular weight, $\mu = 2.3$, for the conversion between n and ρ . This μ value reflects the condition that the major component is H_2 molecules.

We take into account the ionization by Galactic cosmic rays and X-rays from a central star. The total ionization rate, ξ , is the sum of these two sources,

$$\xi = \xi_{\text{CR}} + \xi_{\text{X}}, \quad (7)$$

where subscripts CR and X represent cosmic rays and stellar X-rays, respectively. We adopt $\xi_{\text{CR}} = 10^{-17} \exp(-l/l_{\text{cr}}) \text{ s}^{-1}$, where l is the column densities integrated from the upper or lower surfaces and $l_{\text{cr}} = 100 \text{ g cm}^{-2}$ is the path length of cosmic rays (Hayashi 1981; Turner, Sano, & Dziourkevitch 2007).

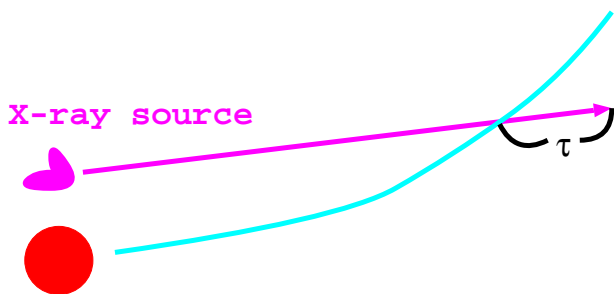


FIG. 4.— The path, ds , of emitted X-ray from the source located above a central star to the disk (pink line). The blue line is the upper disk surface. (see text)

Observations of T-Tauri stars show high X-ray activities. The typical luminosity in X-ray wavelength is $10^{29-31} \text{ erg s}^{-1}$, which is 3-5 orders of magnitude higher than the level of the present Sun (e.g. Telleschi et al. 2007). These X-rays are supposed to be an efficient ionization source. Following Glassgold, Najita, & Igea (1997), we model the ionization rate, ξ_{X} , by the X-rays. We assume the X-ray sources located at $10 R_{\odot}$ ($\sim 3 - 5$ stellar radii) above and below a star, where R_{\odot} denotes the solar radius. The X-ray follows the path shown in Figure 4. The ionization rate is obtained by Glassgold, Najita, & Igea (1997); Fromang, Terquem, & Balbus (2002) as follows:

$$\xi_{\text{X}}/J(\tau) = 1.2 \times 10^{-11} (\text{cm}^{-2} \text{ s}^{-1})$$

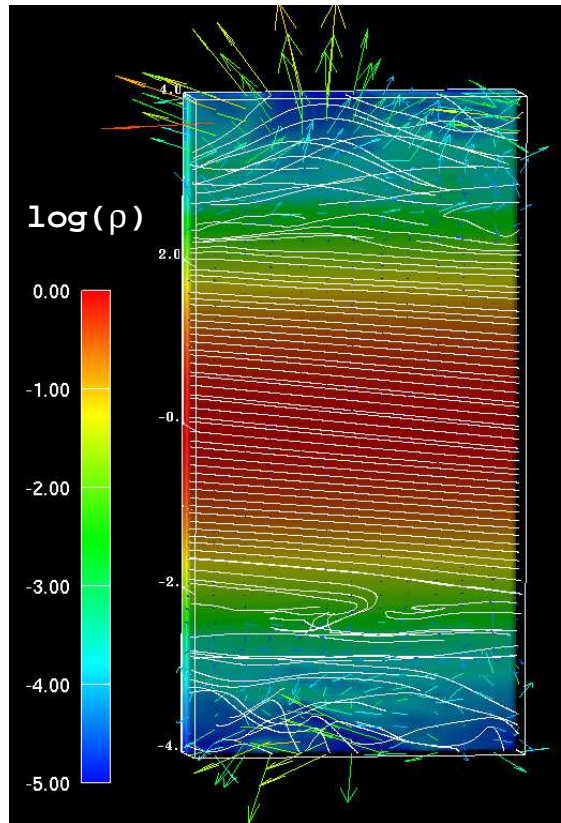


FIG. 5.— Snap-shot of the local disk with dead zone at 250 rotations in the case with medium X-ray activity at 1 AU. The colors indicate the logarithmic scale of density, the solid lines represent magnetic fields, and the arrows are velocity field.

$$\times \left(\frac{L_{\text{X}}}{10^{30} \text{ erg s}^{-1}} \right) \left(\frac{r}{1 \text{ AU}} \right)^{-2} \left(\frac{\sigma}{4 \times 10^{-24} \text{ cm}^2} \right), \quad (8)$$

where L_{X} is the X-ray luminosity, $\sigma \approx 4 \times 10^{-24} \left(\frac{E_{\text{X}}}{3 \text{ keV}} \right)^{-2.81}$ is the absorption cross section depending on the X-ray energy, E_{X} , $\tau = \int ds n \sigma$ is optical depth and $J(\tau) = 0.686 \tau^{-0.606} \exp(-1.778 \tau^{0.262})$. Here, the optical depth, τ , is integrated along the path, ds , in Figure 4 for the variation of scale height, $H \approx 0.05 \text{ AU} \left(\frac{r}{1 \text{ AU}} \right)^{5/4}$.

We perform simulations at three different locations, $r = 1, 5, 25 \text{ AU}$. We consider the three levels of X-ray activities : $(L_{\text{X}}(\text{erg s}^{-1}), E_{\text{X}}(\text{keV})) = (10^{31}, 5)$, $(10^{30}, 3)$, and $(10^{29}, 1)$, which we call the strong, medium, and weak X-ray cases, respectively. We adopt the original MMSN for the surface density, $\Sigma = 1700 \text{ g cm}^{-2} \left(\frac{r}{1 \text{ AU}} \right)^{-3/2}$. In the resistive MHD simulations we adopt the only standard resolution $((x, y, z) = (\pm 0.5H, \pm 2H, \pm 4H))$ is resolved by $(32, 64, 256)$ grid points). We impose weak net vertical magnetic field, $\beta_{z, \text{mid}} = 10^6$, at the midplane. The constant $\beta_{z, \text{mid}}$ distribution indicates that we assume the dependence of the net vertical field of $\langle B_z \rangle \approx 0.01 \text{ G} \left(\frac{r}{1 \text{ AU}} \right)^{-13/8}$ for the MMSN ($\rho_{\text{mid}} \propto r^{-11/4}$ and $c_s \propto r^{-1/4}$).

2.3.2. Result

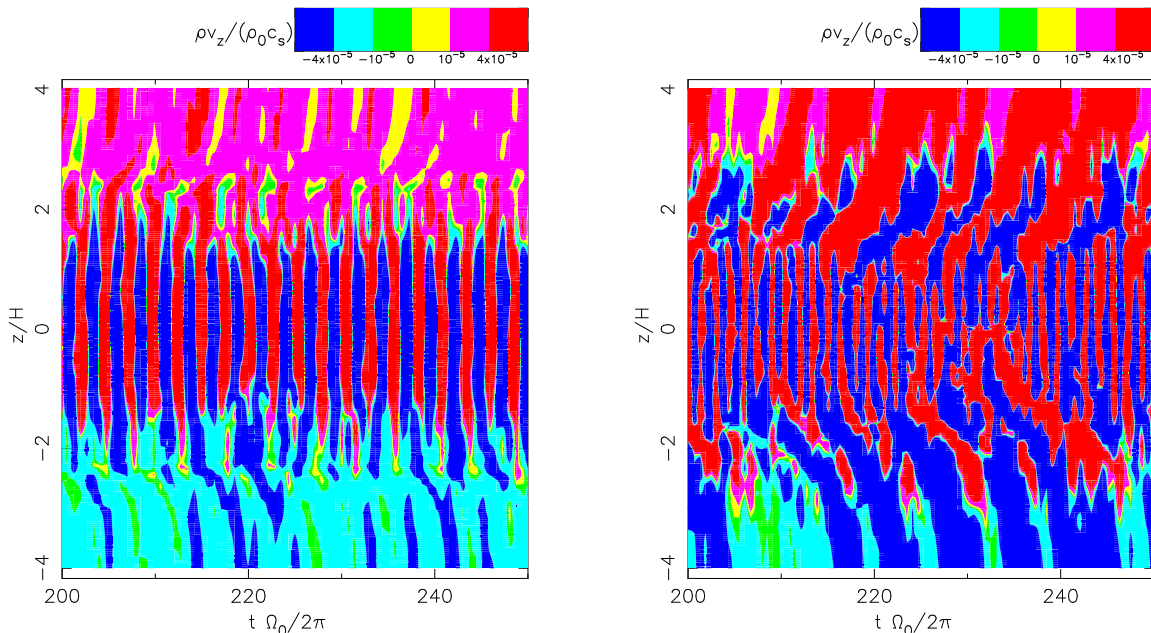


FIG. 6.— Comparison of time-height diagram of ρv_z between the resistive MHD case of the medium X-ray ($L_X = 10^{30}$ erg s $^{-1}$ and $E_X = 3$ keV) at 1 AU (left panel) and the ideal MHD case (right panel). ρv_z is averaged over the $x - y$ planes. The horizontal axis is in unit of rotation period, and the vertical axis is normalized by scale height, $H = \sqrt{2}c_s/\Omega$.

First, we describe results of the case with the medium X-ray activity at 1 AU in detail before discussing results of the different locations and X-ray activities. Figure 5 shows a snapshot of the local disk structure at 250 rotations. (Note that the density is in *logarithmic* scale here; *c.f.*, a linear scale was used in Figure 1.) The figure shows that the magnetic field lines become almost straight in the dead zone, $-2H \lesssim z \lesssim 2H$, because MRI does not operate due to the insufficient ionization here. This is a clear contrast to disks without dead zones (Figure 1; see also SI09). In the surface regions, however, the magnetic fields are more turbulent because the ionizing cosmic rays and X-rays can penetrate to these regions and MRI is active at $r \approx \pm(2 - 3)H$. One can also see that the disk winds stream out of both surfaces because the disk winds are driven from the surface regions with sufficient ionization rather than a deeper midplane location. The breakups of the channel flows triggered by MRI at $z \approx 2H$ and Parker instability in $z \gtrsim 3H$ drive these disk winds, as explained in §2.1. For example, one can see a typical \supset -shape channel flow structure at $z \simeq -2H$, and a \frown -shape structure at $z \simeq (3 - 4)H$, which is typical for Parker instability. Although the mass flux of the disk winds become moderately smaller than the ideal MHD run, the dead zone give little effects on the disk winds (see below).

Figure 6 compares the time-height diagrams of the mass flux, ρv_z of the same case (left panel) to the result of the ideal MHD case (right panel). ρv_z is averaged over the $x - y$ planes at each time step. The left panel shows that disk winds flow out of the upper and lower surfaces even though the dead zone forms around the midplane. This is because the disk winds are excited from the surface regions, which we called injection regions in SI09, with the sufficient ionization, rather than deeper locations near the midplane. These injection regions

are a consequence of the breakups of large-scale channel flows. The disk winds flow out intermittently with quasi-periodicity of 5-10 rotations owing to the quasi-periodic breakups of the channel flows. The recurrent nature of the disk winds universally holds in both cases with and without dead zones, which might explain observed time-variabilities of protostar–protoplanetary disk systems (Wisniewski et al. 2009; Muzerolle et al. 2009; Bary, Leisenring, & Skruskie 2009). The heights of the injection regions become slightly higher than those of the ideal MHD case because the ionization degree at the deeper locations is not sufficient for MRI. Accordingly the mass flux of disk winds from the dead zone case is a little smaller than that of the no dead zone case.

Figure 7 compares the vertical structure of these cases averaging over 200 rotations after the quasi-steady states are achieved. α_z in the lower right panel is the average of α (Equation 2) on each $x - y$ plane. The right panels (magnetic energy and α values) show that the dead zone extends from $z = -2H$ to $2H$ in the resistive MHD case. α_z sharply declines at $z = \pm 2H$ from the surface regions toward the midplane. It is expected that the mass accretion mainly takes place in the surface regions (Gammie 1996). The averaged α value, $\bar{\alpha} (= \int dz \rho \alpha_z / \Sigma)$, which directly determines global mass accretion rate, of the dead zone case is $\sim 3 \times 10^{-4}$, while it is ≈ 0.011 in the no dead zone case (Figure 2). On the other hand, in the surface regions the magnetic energy and α_z of the resistive MHD case are similar to those of the ideal MHD case because the sufficient ionization is achieved there by the X-rays and cosmic rays from the surfaces. The disk winds are effectively accelerated from the injection regions, and the velocity structures are very similar in both cases (the upper left panel of Figure 7). The density of the winds are smaller because the heights of the injection regions are slightly higher in the dead zone case. Accordingly, the

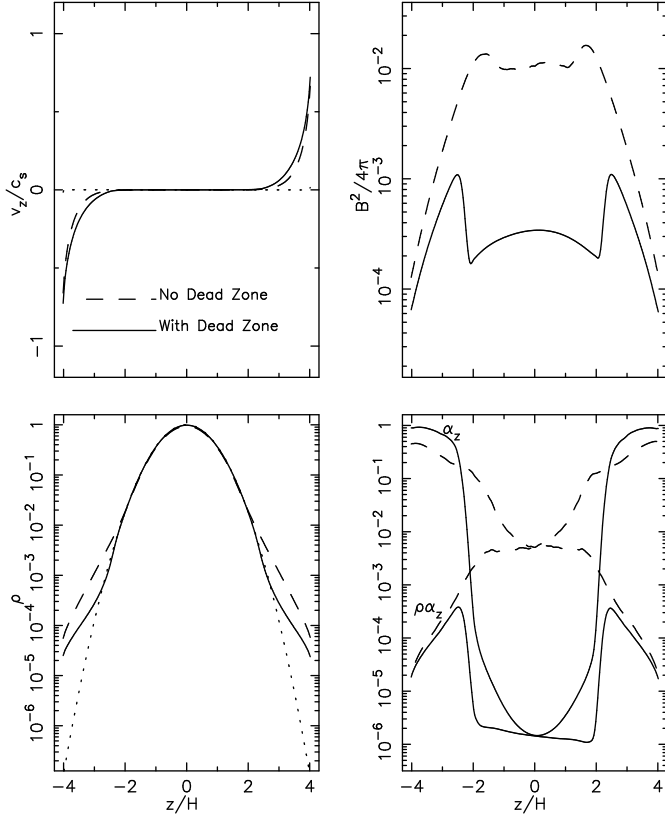


FIG. 7.— Comparison of the resistive MHD (dead zone) case of the medium X-rays at 1AU (solid lines) with the ideal MHD (no dead zone) case (dashed lines). Both cases assume the net vertical magnetic field with $\beta_{z,\text{mid}} = 10^6$. The horizontal axis is vertical height in unit of $H (= \sqrt{2c_s/\Omega})$. The upper left panel shows the vertical velocities normalized by the sound speed; the lower left panel shows the densities; the upper right panel shows the magnetic energy. The lower right panel shows α_z and $\rho\alpha_z$.

mass flux of disk winds of the resistive MHD case is the half of the mass flux of the ideal MHD case.

Figure 8 summarizes the averaged turbulent viscosities, $\bar{\alpha}$, and the mass fluxes of the disk winds for the different locations and X-ray activities. The figure illustrates that both $\bar{\alpha}$ and C_w are smaller in the inner regions. Since surface density is larger for smaller r , ionizing cosmic rays and X-rays cannot reach the midplane in the inner disk. A large fraction is occupied by the dead zone in the inner parts of disks. The $\bar{\alpha}$ values are reduced by more than an order of magnitude at $r = 1$ AU. On the other hand, C_w is not so reduced, being half at most at $r = 1$ AU, because the disk winds are excited from the surface regions and not so affected by the dead zones.

3. GLOBAL MODELING

We solve the time-evolution of surface density with mass accretion and disk wind mass loss (e.g. Alexander, Clarke, & Pringle 2006):

$$\frac{\partial \Sigma}{\partial t} - \frac{1}{r} \frac{\partial}{\partial r} \left[\frac{2}{r\Omega} \frac{\partial}{\partial r} (\Sigma r^2 \alpha c_s^2) \right] + (\rho v_z)_w = 0. \quad (9)$$

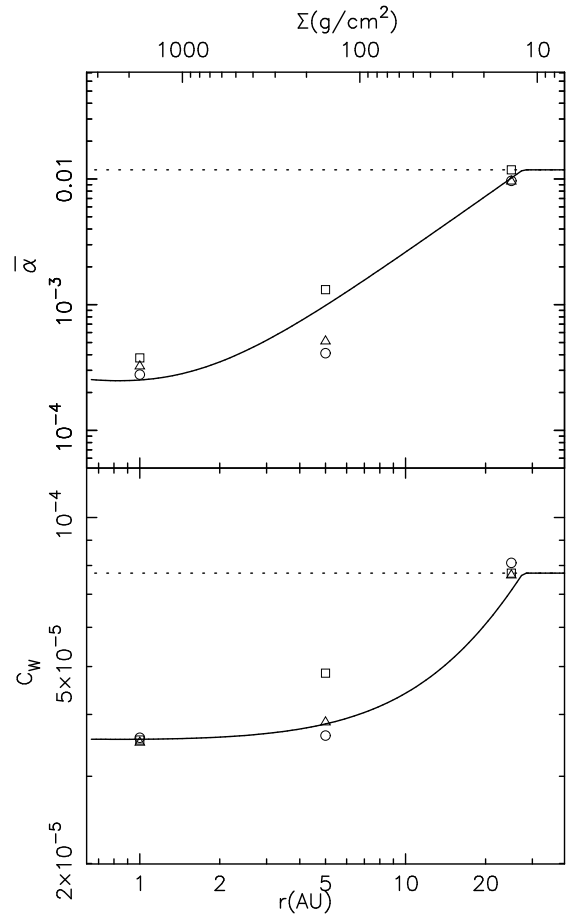


FIG. 8.— Turbulent viscosity, $\bar{\alpha}$, (top) and disk wind mass flux, $C_w (= (\rho v_z)_w / (\rho_{\text{mid}} c_s))$, (bottom) of the resistive MHD simulations at different locations. The squares are the results of the strong X-ray cases ($L_X = 10^{31}$ erg s $^{-1}$, $E_X = 5$ keV), the triangles are the results of the medium X-ray cases ($L_X = 10^{30}$ erg s $^{-1}$ and $E_X = 3$ keV), and the circles are the results of the weak X-ray cases ($L_X = 10^{29}$ erg s $^{-1}$ and $E_X = 1$ keV). The solid lines are the fitting formula (Equations 14 and 16) used for the global calculations. The dotted lines are the results of ideal MHD simulations with net vertical field, $\beta_{z,\text{mid}} = 10^6$.

The second term denotes the radial mass flow by turbulent viscosity. Here and from now, we simply write α for the turbulent viscosity in the global models, which is adopted from $\bar{\alpha}$ of the shearing box simulations of the previous section. The third term is the mass loss by disk winds, where we here assume the specific angular momentum carried in the disk winds is the same as that in the disk material. Both α and $(\rho v_z)_w$ are adopted from the local 3D MHD simulations in §2.2 and 2.3.

We assume the temperature structure of the MMSN (Equation 6). The initial surface density profile is also adopted from the MMSN,

$$\Sigma = f_g \Sigma_0 \left(\frac{r}{1 \text{ AU}} \right)^{-3/2} \exp(-r/r_{\text{cut}}), \quad (10)$$

where $\Sigma_0 = 2400$ g cm $^{-2}$ at 1 AU ($f_g = 0.7$ for the original Hayashi MMSN) and we use a cut-off radius, $r_{\text{cut}} = 50$ AU. Although in the local resistive MHD simulations for dead zones (§2.3) we adopted the original MMSN value, $f_g \Sigma_0 = 1700$ g cm $^{-2}$, a specific choice of f_g in the local simulations does not change the results of

the global disk because we explicitly take into account the dependences of α and C_w on Σ (§3.2).

We integrate Equation (9) by using the nondimensionalized variables in unit of $r_0 = \Omega_0 = f_g \Sigma_0 = 1$, so the scaling factor, f_g , does not appear explicitly in the calculations. The calculation region⁵ is from $r_{\text{in}} = 0.01$ AU to $r_{\text{out}} = 10000$ AU which is resolved by 2000 mesh points with grid spacing in proportion to \sqrt{r} .

3.1. Disks without Dead Zone

We apply the α and C_w obtained in the local ideal MHD simulations (§2.2 and Figure 2) to the global model. Figure 2 can be regarded as a time sequence along with disk evolution because the surface density of protoplanetary disks decreases while vertical magnetic flux is supposed to be rather kept constant. If initial vertical magnetic fields are zero or very weak ($\beta_{z,\text{mid}} \gg 10^7$), α and C_w are expected to stay almost constant even after surface density decreases considerably. For such situations, we use constant $\alpha = \alpha_{\text{fl}} = 8 \times 10^{-3}$ and $C_w = C_{w,\text{fl}} = 2 \times 10^{-5}$ (solid lines in Figure 2), which are the floor values obtained by the local simulations. For the disk wind mass flux, we choose a conservative value because the actual mass flux might be moderately smaller by returning mass from higher altitudes (§5.1 and 5.4).

When C_w stays constant, the disk wind flux has the following scaling :

$$(\rho v_z)_w = C_w \rho_{\text{mid}} c_s \propto \Sigma r^{-3/2}, \quad (11)$$

where for the last proportionality we use $\rho_{\text{mid}} c_s \propto \Sigma \Omega$ and assume a Keplerian rotating disk. Equation (11) shows that the wind mass flux is larger for smaller r , and the dispersal of protoplanetary disks by the disk winds starts from the inner part.

If initial vertical fields are not so weak, α and C_w eventually increase when $\beta_{z,\text{mid}} \gtrsim 10^5$ (Figure 2). In order to take into account this effect we adopt the following prescription :

$$\alpha = \alpha_{\text{fl}} \times \max\left(1, \frac{\Sigma_{\text{up}}(r)}{\Sigma(r)}\right), \quad (12)$$

and

$$C_w = C_{w,\text{fl}} \times \max\left(1, \frac{\Sigma_{\text{up}}(r)}{\Sigma(r)}\right), \quad (13)$$

where Σ_{up} is the surface density at which α and C_w start to increase in Figure 2 ($\beta_{z,\text{mid}} \sim 10^5$). Σ_{up} is determined by the initial vertical magnetic flux. We model $\Sigma_{\text{up}}(r) = \delta_{\text{up}} \Sigma_{\text{init}}(r)$; α and C_w starts to increase when the surface density decreases to δ_{up} of the initial value. For simplicity, we assume a constant $\delta_{\text{up}} = 0.01$ in this paper.

We calculate the three cases for the disks without dead zones summarized in Table 1 (Models I – III). In Models

⁵ Our results are not affected by the location of r_{in} . The adopted value, $r_{\text{in}} \approx 2R_{\odot}$, roughly coincides a typical radius of T-tauri stars, where R_{\odot} is the solar radius. In realistic situations, however, a disk may truncate at several stellar radii where the Keplerian rotation frequency equals to the rotation frequency of the corotating stellar magnetic field (Ghosh & Lamb 1979). The matter can directly accrete to a central star through connecting flux tubes (Kenyon, Yi, & Hartmann 1996).

Model	Disk Wind	net B_z	Dead Zone
I	No	Weak/No	No
II	Yes	Weak/No	No
III	Yes	Strong	No
IV	No	Weak/No	Yes
V	Yes	Weak/No	Yes

TABLE 1
GLOBAL MODELS.

II and III we take into account the disk winds; Model II adopts the constant α & C_w to model weak vertical magnetic fields and Model III prescribes Equations (12) and (13) to incorporate relatively strong vertical fields.

3.2. Disks with Dead Zones

We apply the results of the local resistive MHD simulations (§2.3 and Figure 8) to the global model. An essential point is that α and C_w can be determined by r and Σ . Then, we use the following parameterization :

$$\alpha = \alpha_{\text{fl}} \frac{\Sigma_{\text{act}}}{\Sigma}, \quad (14)$$

where Σ_{act} is the sum of the column density of active regions near upper and lower disk surfaces which is modeled as

$$\Sigma_{\text{act}} = \min\left(\Sigma_{\text{CR}} + \Sigma_{\text{X}} \left(\frac{r}{1\text{AU}}\right)^{-2}, \Sigma\right), \quad (15)$$

where Σ_{CR} is the column density with sufficient ionization by cosmic rays, and Σ_{X} is the column density with sufficient ionization by X-rays normalized at 1 AU. Σ_{X} has dependence on r^{-2} to take into account the geometrical dilution of the X-ray flux from a central star, while Σ_{CR} is constant because cosmic rays are diffusely distributed. To reproduce the results of the local simulations, we adopt $\Sigma_{\text{CR}} = 12 \text{ g cm}^{-2}$ and $\Sigma_{\text{X}} = 25 \text{ g cm}^{-2}$. The mass flux of disk winds is also reduced in accordance with α , but we set a lower limit to match the local simulation results:

$$C_w = C_{w,\text{min}} + (C_{w,\text{fl}} - C_{w,\text{min}}) \frac{\alpha}{\alpha_{\text{fl}}} \quad (16)$$

where we use $C_{w,\text{min}} = 0.45 \times C_{w,\text{fl}}$.

The solid lines in Figure 8 represent Equations (14) and (16). In the figure we use $\alpha_{\text{fl}} = 0.011$ and $C_{w,\text{fl}} = 7.7 \times 10^{-5}$ for the floor values of the ideal MHD simulations with net vertical field of $\beta_{z,\text{mid}} = 10^6$ (Figure 2). For the global disk calculation we use the original values, $\alpha_{\text{fl}} = 8 \times 10^{-3}$ and $C_{w,\text{fl}} = 2 \times 10^{-5}$.

4. RESULTS OF GLOBAL MODELS

4.1. Evolution of Gas Disks

The top panel of Figure 9 shows the evolution of the surface densities of the no dead zone cases (Models I – III). The result of the no wind case (Model I; black thin lines) follows a self-similar solution of $\Sigma \propto 1/r$ in the inner region with an exponential cutoff in the outer region (Lynden-Bell & Pringle 1974). On the other hand, the disk wind cases (Models II and III; blue thin and red thick lines) shows faster decreases of Σ in the inner regions owing to the contribution from the disk winds in addition to the accretion. The figure clearly shows that

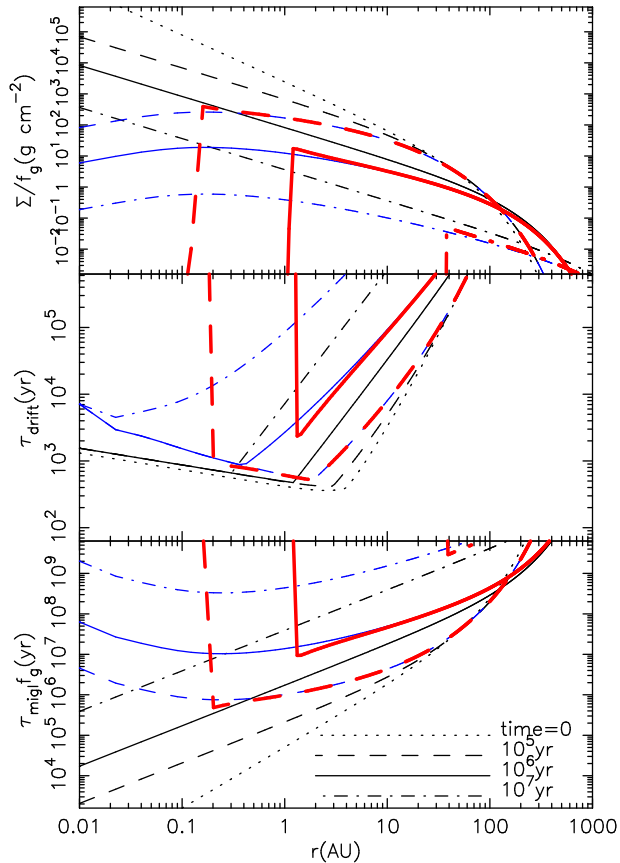


FIG. 9.— The results of the no dead zone cases (Models I – III). From top to bottom, time evolution of disk surface density, Σ , timescale, τ_{drift} , of inward drift of a m-size boulder, and timescale, $\tau_{\text{mig,I}}$, of type I migration of an Earth-mass planet are shown. The black thin lines are the results without disk winds (Model I); the blue thin lines are the results with disk winds for weak/no vertical magnetic fields (Model II); the red thick lines are the results with disk winds for relatively strong net vertical fields (Model III). The dotted lines are the initial values. The dashed, solid, and dot-dashed lines are the results at 10^5 , 10^6 , and 10^7 yrs. Note that Σ and $\tau_{\text{mig,I}}$ can be scaled by f_g . For example, the case with $f_g = 2$ gives twice larger Σ and smaller $\tau_{\text{mig,I}}$ than the case with $f_g = 1$. The results of τ_{drift} are for $f_g = 1$, because this scaling cannot be applied to τ_{drift} . The bending points of τ_{drift} correspond to the change of the regimes of drag force. The inside region corresponds to the Stokes regime where the dust size is larger than the mean free path of a gas particle, and the outside region corresponds to the Epstein regime where the dust size is smaller than the mean free path of a gas particle.

the dispersal of the gas disk takes place in an inside-out manner, as discussed above (Equation 11).

The case with relatively strong vertical net magnetic flux (red lines) shows an expanding inner hole because the surface density decreases to reach $\delta_{\text{up}} (= 0.01)$ of the initial values faster in the inner regions and α and C_w start to increase from inner to outer locations. Although the quantitative properties of evolving inner holes depends on the adopted parameters (see §2.2), the observed properties of transitional disks with inner holes (Calvet et al. 2005; Espaillat et al. 2008; Hughes et al. 2009) may be explained by the mechanism presented here.

The top panel of Figure 10 shows the evolution of the surface densities of the dead zone cases. The results of Models IV & V exhibit density enhancements, which correspond to the dead zones. Because the surface densities

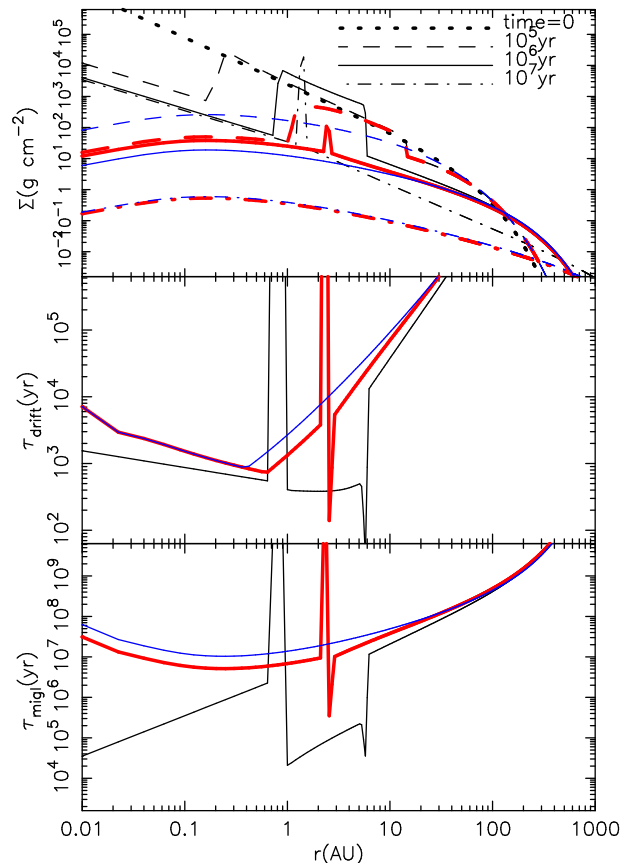


FIG. 10.— Comparison of the dead zone cases with the no-dead zone case. The black, red, and blue lines are the results of Models IV (dead zone / no disk wind), V (dead zone / disk wind), and II (no dead zone / disk wind), respectively. The top panel compares the time evolution of surface density, Σ . The dotted, dashed, solid, and dot-dashed lines are the results at $t = 0$, 10^5 , 10^6 , and 10^7 yrs. The middle panel compares the inward drift timescales, τ_{drift} , of a m-size boulder at $t = 10^6$ yr. The bottom panel compares the timescale, $\tau_{\text{mig,I}}$, of type I migration of an Earth-mass planet at $t = 10^6$ yr.

in these regions are high, the X-rays and cosmic rays cannot penetrate to the midplanes. The dead zones form around the midplanes, and α and C_w become smaller. Smaller α leads to slower mass accretion⁶, and then, the mass accumulates around the dead zones, which is observed as the density enhancements. Without disk winds, the dead zone exists until 10^7 yr (Model IV; black lines).

On the other hand, when taking into account the disk winds, the dead zone almost disappears at 10^6 yr (Model V; red lines) because the surface density decreases faster owing to the disk winds, which further leads to the effective penetration of the ionizing X-rays and cosmic rays to the midplane. After the dead zone disappears, the disk evolution follows the no dead zone case. The surface density structure in later times (e.g. at 10^7 yr in the figure) is very similar to that of the no dead zone case (Model II; blue lines). We can conclude that the MRI-driven disk winds play an essential role in the dispersal of protoplanetary gas disks even though the dead zone forms.

⁶ The disk expands around the outer edge of the dead zone, while the mass accretes in the rest of the dead zone region.

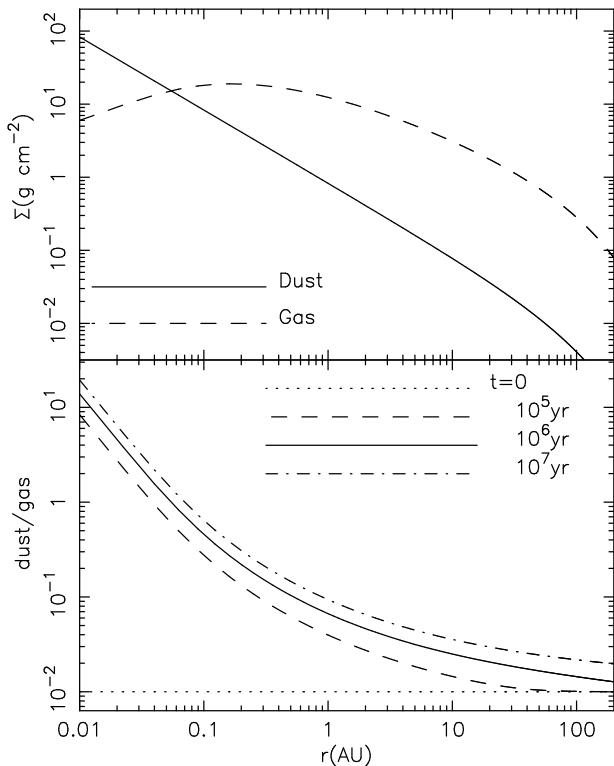


FIG. 11.— *Upper*: Surface density of dust (solid) and gas (dashed) components at $t = 10^6$ yr. *Lower*: Dust-to-gas ratios at $t = 10^5$ yr (dashed), 10^6 yr (solid), and 10^7 yr (dot-dashed). The dotted line is the initial condition (dust-to-gas ratio = 0.01).

4.2. Dynamics of Boulders and Planetesimal Formation

In addition to the dynamical evaporation of protoplanetary gas disks, MRI-driven disk winds affect the planet formation at various stages. At an early stage the rapid infall of boulders to a central star (Weidenschilling 1977), which hinders the growth of solids to larger bodies by aggregation, is a severe problem. The solid component rotates with the Keplerian velocity as a result of the force balance between the gravity due to a central star and the centrifugal force. On the other hand, the gas rotates with sub-Keplerian velocity by the contribution from outward pressure gradient force. Then, the rotation of the solid component is slightly slowed down because of the head-wind from the gas, and drifts inward. Under the typical MMSN condition, the infalling timescale of \sim meter-sized boulders is $\sim 100 - 1000$ years at 1 AU, which is too rapid to form planetesimals (\sim kilometer size) in a turbulent gas disk.

However, our calculations show that the surface density is increasing with r in the inner region (the top panels of Figures 9 and 10). The inward drift rate becomes smaller than previously discussed. The middle panels of Figures 9 and 10 compares the inward drift timescales (Weidenschilling 1977),

$$\tau_{\text{drift}} = r \left(-\frac{1}{\Omega \rho} \frac{dp}{dr} \frac{t_s \Omega}{1 + (t_s \Omega)^2} \right)^{-1}, \quad (17)$$

where t_s is stopping time of solid material in a gas disk. Here we consider a one meter-size spherical boulder for t_s , and the pressure-gradient force ($dp/dr < 0$ for sub-

Keplerian rotating gas disks) is estimated at the midplanes of disks. As expected, τ_{drift} becomes longer when the disk wind is taken into account (Figure 9), which is more favorable for the formation of planetesimals. The tendency is the same for the dead zone cases as well (Figure 10), while τ_{drift} 's show complicated behaviors at the edges of the dead zones reflecting the sharp density gradients.

The dispersal of the gas component directly leads to the increase of a dust-to-gas ratio, which is also important in the context of gravitational instability of dust particles. Sekiya (1998) investigated the turbulence due to shear motions between gas and dust. He found that when a significant fraction of the gas component is dispersed with dusts left, the shear-induced turbulence is reduced and dusts become gravitationally unstable, which possibly leads to the formation of planetesimals (see also Youdin & Shu 2002; Michikoshi & Inutsuka 2006, for related works). Johansen et al. (2007) also proposed that streaming instability triggers the direct formation of large planetesimals or dwarf planets when the dust-to-gas ratio increases to an order of unity. The disk winds disperse the gas component selectively and raise the dust-to-gas ratio in an inside-out manner, which activates streaming instability from inner regions.

To illustrate the increase of the dust-to-gas ratio, we calculate the time-evolution of dust surface density by using the same global model. Here, we assume that dust particles follow the only viscous accretion with gas near the midplane and do not escape with disk winds; we solve Equation (9) by setting $(\rho v_z)_w = 0$ for the dust component. This assumption is reasonable if dust particles are well-coupled with gas near the midplane and decoupled in the upper regions. Nondimensional stopping time, Ωt_s , is a good indicator which measures the coupling between dust and gas; if $\Omega t_s < 1$, dusts are well-coupled with gas, and vice versa. When one takes dust particles with size of millimeter at 1 AU of the MMSN with $f_g = 1$ (Equation 10) as an example, $\Omega t_s \approx 2 \times 10^{-4}$ at the midplane. Since stopping time is inversely proportional to gas density, Ωt_s exceeds unity at $z \approx \pm 3H$ where $\rho/\rho_{\text{mid}} \approx 2 \times 10^{-4}$ (Figure 7). The assumption is reasonable for moderately small dusts (sub-millimeter – meter at 1 AU of the MMSN). Further smaller dusts will be lift up with disk winds, while larger solid particles are decoupled with gas even at the midplane.

We initially impose a uniform dust-to-gas ratio = 0.01 and follow the evolution of both gas and dust with using the parameters of Model II of Table 1. The upper panel of Figure 11 presents the surface densities of dust (solid) and gas (dashed) at $t = 10^6$ yr, which shows that the dust surface density is larger than the gas surface density in the inner region, $r \lesssim 0.1$ AU. The lower panel shows that the dust-to-gas ratio gradually increases from the inner region.

4.3. Type I Migration

After the formation of planets, the gas component in a disk also plays a role in the evolution of the planetary system. A lower-mass planet, which cannot create a gap in a gas disk, resonantly interacts with the gas component of a disk through gravitational torque (Ward 1997). As a result planets generally migrate inward with timescale

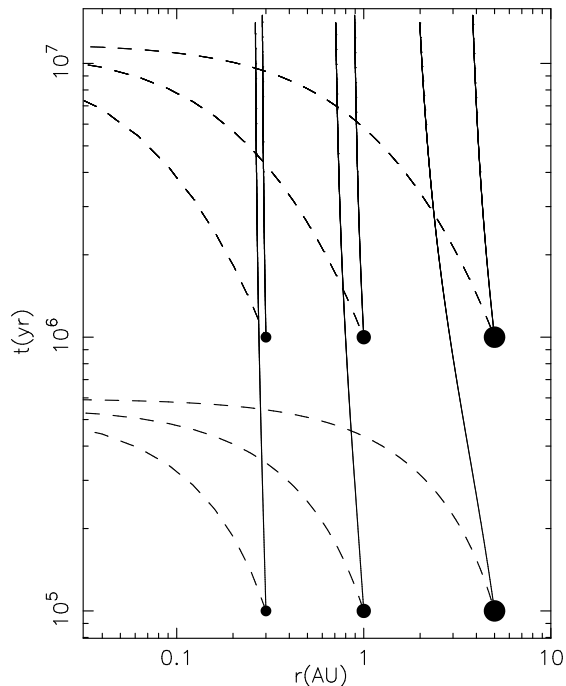


FIG. 12.— Orbital evolution of planets by type I migration. The horizontal axis shows radial distance and the vertical axis shows time elapsed from the starting point of the disk calculation. The solid lines are the results with disk winds (Model II) and the dashed lines are the results without disk wind (Model I). The circles indicate the initial locations of newly formed planets : At $t = 10^5$ yr and 10^6 yr we put planets with $0.3M_{\oplus}$ at 0.3 AU, planets with $1M_{\oplus}$ at 1 AU, and planets with $5M_{\oplus}$ at 5 AU.

(Tanaka, Takeuchi, & Ward 2002),

$$\tau_{\text{mig,I}}(r) \approx 5 \times 10^4 \text{yr} \left(\frac{4.35}{2.7 + 1.1s} \right) \left(\frac{\Sigma(r)}{\Sigma_0} \right)^{-1} \left(\frac{M}{M_{\oplus}} \right)^{-1} \quad (18)$$

where s is the local gradient of $\Sigma \propto r^{-s}$, M is planet mass, M_{\oplus} is the Earth mass, and we assume the MMSN around a central star with the solar mass. This equation indicates that the migration is faster in a more massive (larger Σ) gas disk because of the larger torque on a planet. In typical situations, $\tau_{\text{mig,I}}$ is shorter than the lifetimes of protoplanetary gas disks; newly formed terrestrial planets and cores of gas-giant planets quickly fall into a central star.

However, we have shown that the gas density in the inner regions quickly decreases by the disk winds, and the gradient of surface density becomes positive in the inner region. Consequently, $\tau_{\text{mig,I}}$ becomes considerably longer than previously considered. The bottom panels of Figures 9 and 10 show $\tau_{\text{mig,I}}$ for an Earth-mass planet around a solar-mass star. The figures illustrate that the disk winds greatly suppress the migrations in the inner region both in no dead zone and dead zone cases. Similarly to τ_{drift} , $\tau_{\text{mig,I}}$'s of the dead zone cases show complicated behaviors at the edges of the dead zones (Matsumura, Pudritz, & Thommes 2007; Kato et al. 2009).

To illustrate the suppression of type I migration more clearly, we calculate the migrations of planets with the evolution of protoplanetary disks by using migration speed, $r/\tau_{\text{mig,I}}$ (Figure 12). In the no disk wind case (Model I) all the planets infall to a central star. On the

other hand, in the disk wind case (Model II) the migrations are slow and all the planets survive. When the disk winds are considered, type I migration becomes unimportant especially at later times, $t \gtrsim 10^5 - 10^6$ yr, under the typical MMSN condition.

5. DISCUSSIONS

5.1. Energetics

In this paper we have applied results of the local simulations to the global models. We use the mass flux of the disk winds at the upper and lower boundaries, $z = \pm 4H$, of the simulation box. Since the wind velocities at the boundaries are still smaller than the escape speed from a central star, we should carefully examine whether the disk winds really escape from the disks. In this subsection, we examine the energetics of the disk winds to see whether the accretion energy can potentially drive the disk winds that can escape from the gravity of a central star.

The starting point here is an equation for the conservation of total energy :

$$\begin{aligned} \frac{\partial}{\partial t} \left[\rho \left(\frac{1}{2}v^2 + \frac{1}{\gamma-1} \frac{p}{\rho} - \frac{GM_{\star}}{r} \right) + \frac{B^2}{8\pi} \right] \\ + \nabla \cdot \left[\left\{ \rho \mathbf{v} \left(\frac{1}{2}v^2 + \frac{\gamma}{\gamma-1} \frac{p}{\rho} - \frac{GM_{\star}}{r} \right) \right. \right. \\ \left. \left. + \mathbf{v} \frac{B^2}{4\pi} - \frac{\mathbf{B}}{4\pi} (\mathbf{B} \cdot \mathbf{v}) \right\} \right] = -q_{\text{loss}}, \quad (19) \end{aligned}$$

where q_{loss} is energy loss which is modeled below and here we consider the only r derivative. We integrate Equation (19) with $\int dz$ by neglecting the small terms except the anisotropic stress, $\delta v_{\phi} v_r - B_{\phi} B_r / 4\pi\rho = \alpha c_s^2$, whereas we separate v_{ϕ} into Keplerian rotation plus small perturbation, $v_{\phi} = r\Omega + \delta v_{\phi}$. We also assume that accretion velocity and sound speed ($c_s = \sqrt{\gamma p/\rho}$) are smaller than rotation velocity, $v_r, c_s \ll r\Omega$. Then, the total energy of a ring at r changes according to

$$\frac{\partial}{\partial t} \left[-\Sigma \frac{r^2 \Omega^2}{2} \right] + \frac{1}{r} \frac{\partial}{\partial r} \left[r\Omega \frac{\partial}{\partial r} (r^2 \Sigma \alpha c_s^2) + r^2 \Sigma \Omega \alpha c_s^2 \right] = -Q_{\text{loss}}, \quad (20)$$

where $Q_{\text{loss}} = \int q_{\text{loss}} dz$ and we have used $\frac{GM_{\star}}{r^2} = r\Omega^2$ and $r\Sigma v_r = \frac{2}{r\Omega} \frac{\partial}{\partial r} (r^2 \Sigma \alpha c_s^2)$. The spatial derivative term on the left-hand side represents the energy liberated by mass accretion and viscous heating.

We investigate whether this liberated gravitational energy is sufficient to drive disk winds. For simplicity, we only consider the kinetic energy of disk winds for the loss term and neglect additional effects such as heating by UV/X-ray radiation (energy input), acceleration by stellar winds (momentum input), and radiative cooling (energy loss). Since we consider the disk winds from a Keplerian rotating disk, we can write $Q_{\text{loss}} = \frac{1}{2} \rho v_z (v_z^2 + r^2 \Omega^2)$. Disk winds can escape to infinity if v_z exceeds the escape

speed, $v_{\text{esc}} = \sqrt{2}r\Omega$; namely if the condition,

$$\frac{\partial}{\partial t} \left[\Sigma \frac{r^2 \Omega^2}{2} \right] - \frac{1}{r} \frac{\partial}{\partial r} \left[r \Omega \frac{\partial}{\partial r} (r^2 \Sigma \alpha c_s^2) + r^2 \Sigma \Omega \alpha c_s^2 \right] - \frac{3}{2} (\rho v_z)_w r^2 \Omega^2 \geq 0 \quad (21)$$

is satisfied, disk winds can be driven solely by the liberated gravitational energy of accretion, because the left-hand side of Equation (21) is the energy flux of disk winds at infinity. The time derivative term in Equation (21) can be eliminated by using Equation (9). Then, using the relation of Keplerian rotation, $\Omega \propto r^{-3/2}$, Equation (21) is rewritten as

$$\frac{3}{2} \Omega \Sigma \alpha c_s^2 \geq 2r^2 \Omega^2 (\rho v_z)_w, \quad (22)$$

or more specifically,

$$r \geq \frac{8}{9\pi} \frac{C_w^2 (r_0 \Omega_0)^4}{\alpha^2 c_{s,0}^4} r_0 \equiv r_{\text{dw}}, \quad (23)$$

where we are using Equation (4) and the relation of the MMSN ($c_s \propto r^{-1/4}$) with Keplerian rotation. Substituting the standard values, $\alpha = 8 \times 10^{-3}$ and $C_w = 2 \times 10^{-5}$, in the global model we have $r_{\text{dw}} = 1.4$ AU.

The disk winds in the inner region, $r < r_{\text{dw}}$, do not have sufficient energy to escape from a disk by accretion. The fates of these wind materials are (i) accreting directly to a central star if the angular momentum is removed, (ii) blown away by the stellar winds (see §5.4.3), or (iii) returning back to the disk (see Figure 18 for the schematic picture). If the most of the wind gas follows the processes (i) or (ii), our calculations in §4 give the correct surface gas densities. On the other hand, if the process (iii) is dominant, we overestimate the escaping mass flux of the disk winds. We further discuss the escape of the disk winds in §5.4.

5.2. Global Modeling with Energetics

We can take into account the energetics argument (§5.1) in the global model. We adopt the following limiter for disk wind mass flux, C_w :

$$C_w = \min(C_{w,\text{fl}}, C_{w,\text{eng}}), \quad (24)$$

where $C_{w,\text{eng}}$ corresponds to the mass flux that gives the left-hand side of Equation (21) equal to zero, namely

$$C_{w,\text{eng}} = \left\{ \frac{\partial}{\partial t} \left[\Sigma \frac{r^2 \Omega^2}{2} \right] - \frac{1}{r} \frac{\partial}{\partial r} \left[r \Omega \frac{\partial}{\partial r} (r^2 \Sigma \alpha c_s^2) + r^2 \Sigma \Omega \alpha c_s^2 \right] \right\} \left[\frac{3}{2} r^2 \Omega^2 \rho_{\text{mid}} c_s \right]^{-1}. \quad (25)$$

Equation (24) reduces the mass flux in $r < r_{\text{dw}}$ to the value available from the liberated gravitational energy by accretion. In $r \geq r_{\text{dw}}$, Equation (24) gives $C_w = C_{w,\text{fl}}$.

Figure 13 displays the results which take into account the limiter for C_w (thick red lines) in Model II, in comparison with Model I (no disk wind; black thin lines) and

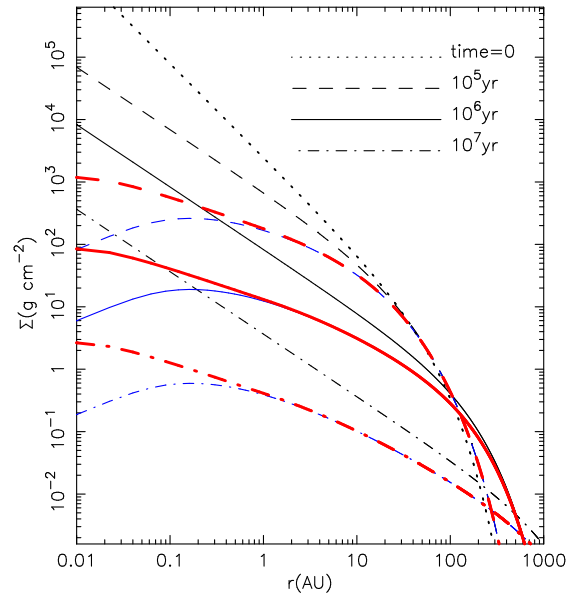


FIG. 13.— Time evolution of disk surface density. The black thin lines are the results without disk winds (Model I); the blue thin lines are the results with the disk winds of the constant mass flux, $C_w = C_{w,\text{fl}}$ (Model II); the red thick lines the results with the disk winds which take into account the energetics limiter for C_w (Equation 24). The dotted lines are the initial values. The dashed, solid, and dot-dashed lines are the results at 10^5 , 10^6 , and 10^7 yrs.

Model II (constant C_w ; blue thin lines). As expected, the difference between the red and blue lines appears only in $r < r_{\text{dw}} (= 1.4$ AU), the surface densities in the outer region are the same. Although the surface density in the inner region becomes larger in the case with the C_w limiter, it is still much lower than the surface density of the no wind case. Then, the disk winds still play an essential role in the dispersal of protoplanetary disks even though taking into account the energetics of the disk winds.

5.3. Mass Loss Rate

Figure 14 shows the mass accretion rate, \dot{M}_r , and the mass loss rate of disk winds, \dot{M}_z , which are respectively defined as

$$\dot{M}_r = -2\pi r \Sigma v_r, \quad (26)$$

and

$$\dot{M}_z(r) = 2\pi \int_r^{r_{\text{out}}} r' dr' (\rho v_z)_w. \quad (27)$$

In the case with disk winds, the mass accretion rate decreases for decreasing r because the mass is lost by the disk winds. The total mass loss rate by the disk winds is $\dot{M}_z(r_{\text{in}}) = 2.5 \times 10^{-9} M_\odot \text{ yr}^{-1}$ and the mass loss rate from $r > r_{\text{dw}}$ that can be accelerated to infinity by accretion energy is $\dot{M}_z(r_{\text{dw}}) = 1.4 \times 10^{-9} M_\odot \text{ yr}^{-1}$; more than the half of the total wind mass loss can escape from the disk by the liberated gravitational energy. The mass loss by the disk winds is larger than the accretion rate. Assuming the truncation of the disk at 5-10 stellar radii (~ 0.1 AU), $\dot{M}_r \approx 2 \times 10^{-10} M_\odot \text{ yr}^{-1}$, which can be regarded as the mass accretion rate through magnetic flux tubes directly connecting to the central star (Kenyon, Yi, & Hartmann 1996).

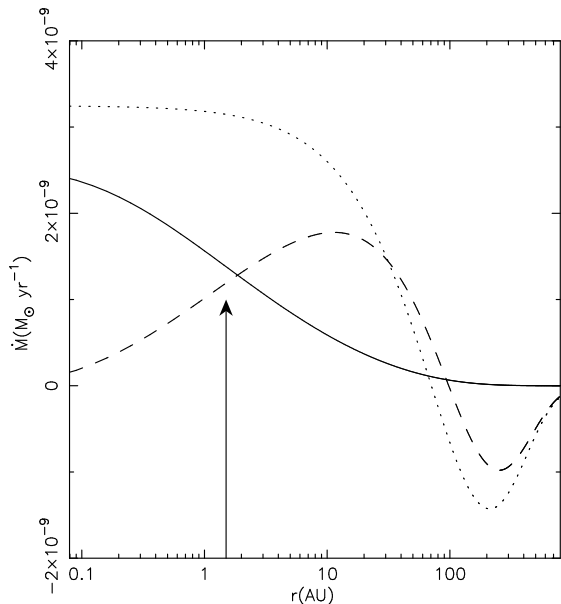


FIG. 14.— Structure of mass loss/accretion rates of Model II in the main paper at $t = 10^6$ yr. The solid line is the mass loss by the disk winds (Equation 27) and the dashed line is the mass accretion rate (Equation 26) of the model taking into account the disk winds. The dotted line is the mass accretion rate of the model without disk winds for comparison. The arrow indicates the location of r_{dw} .

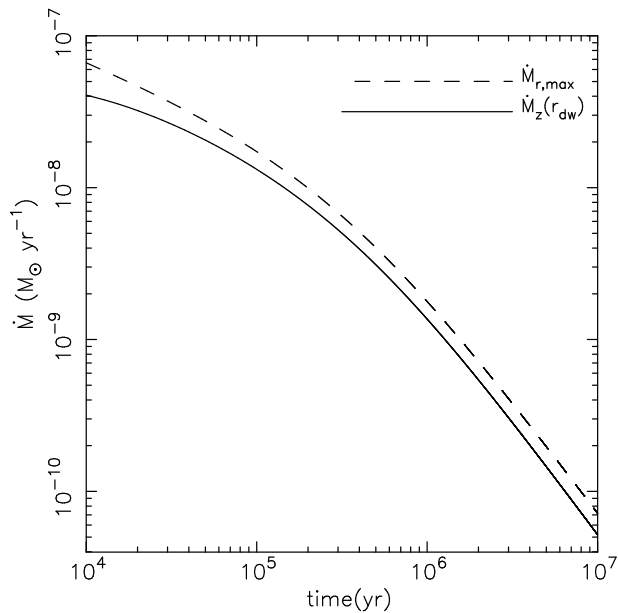


FIG. 15.— Time evolution of the mass loss rate of the disk wind (solid) and accretion rate (dashed) of Model II. Here, the wind mass loss rate is the integration of $r > r_{\text{dw}}$, $\dot{M}_z(r_{\text{dw}})$, that can potentially escape from a central star gravity by accretion energy. The shown accretion rate is the maximum value at each time (e.g. for $t = 10^6$ yrs in Figure 14, the maximum accretion rate is obtained at $r \approx 15$ AU).

The obtained mass loss rate by the MRI-driven disk winds is larger than the mass loss rate, $\lesssim 10^{-10} - 10^{-9} M_{\odot} \text{ yr}^{-1}$, predicted by the UV photoevaporation (e.g. Matsuyama et al. 2003). Recently, photoevaporation by X-rays from a central star is also proposed. It is reported

that the mass loss rate due to X-rays may be larger than that by the UV photoevaporation, where the calculated mass loss rates are rather uncertain (Ercolano, Clarke, & Drake 2009; Gorti, Dullemond, & Hollenbach 2009; Owen et al. 2010). Significant difference of the disk wind mass loss from the photoevaporation processes by UV or X-rays is time evolution. The mass loss rate by the disk winds is correlated with the accretion rate (Figure 15), because the energy source of the disk winds is the gravitational energy liberated by accretion. Therefore, the wind mass loss rate is larger at earlier times when the accretion rate is larger; the disk winds significantly contribute to the dispersal of the gas component of a disk from the beginning. As a result, an inner hole forms from the early epoch and its size is gradually expanding. On the other hand, the UV photoevaporation mechanism is significant at the later times after the sufficient mass dissipates by accretion. Therefore, an inner hole is anticipated at later time when the evaporating mass flux becomes comparable to the mass accretion rate (Alexander et al. 2006). The X-ray photoevaporation, which may be effective from slightly earlier time, is also expected to give the similar trend to the UV photoevaporation (Gorti, Dullemond, & Hollenbach 2009).

5.4. Escape of Disk Winds

We further continue the discussions on the escape of disk winds.

5.4.1. Local Simulations with Larger Vertical Boxes

In order to study the acceleration of the disk winds at higher altitudes, we perform the local 3D MHD simulations with larger vertical boxes. We here use the realistic vertical gravity,

$$g_z = \frac{GM_{\star}z}{(r^2 + z^2)^{3/2}} = \Omega^2 z \frac{r^3}{(r^2 + z^2)^{3/2}}, \quad (28)$$

where r is radial location from a central star. In the usual local simulations, the only leading term, $g_z \simeq \Omega^2 z$, is considered, because r does not appear explicitly and it can be treated more easily (Hawley et al. 1995). On the other hand, the escape velocity is not defined at the expense of the simplification, and the vertical gravity is overestimated by a factor of $\frac{r^3}{(r^2 + z^2)^{3/2}}$, which makes density at a high altitude unrealistically lower. To avoid these shortcomings we use Equation (28) by explicitly setting r (Table 2). Note that $r = 20H$ corresponds to the location of $r \approx 1$ AU for the MMSN. In these runs, we set the net vertical fields with $\beta_{z,\text{mid}} = 10^6$ at the midplanes.

Model	r	Box Size
II(Reference)	—	$-4H < z < 4H$
VI	20	$-6H < z < 6H$
VII	20	$-8H < z < 8H$
VIII	10	$-12H < z < 12H$

TABLE 2
RADIAL POSITIONS AND VERTICAL BOX SIZES OF THE LOCAL SIMULATIONS.

Figure 16 compares the time averaged vertical structures of these cases (Table 2). The top left panel shows

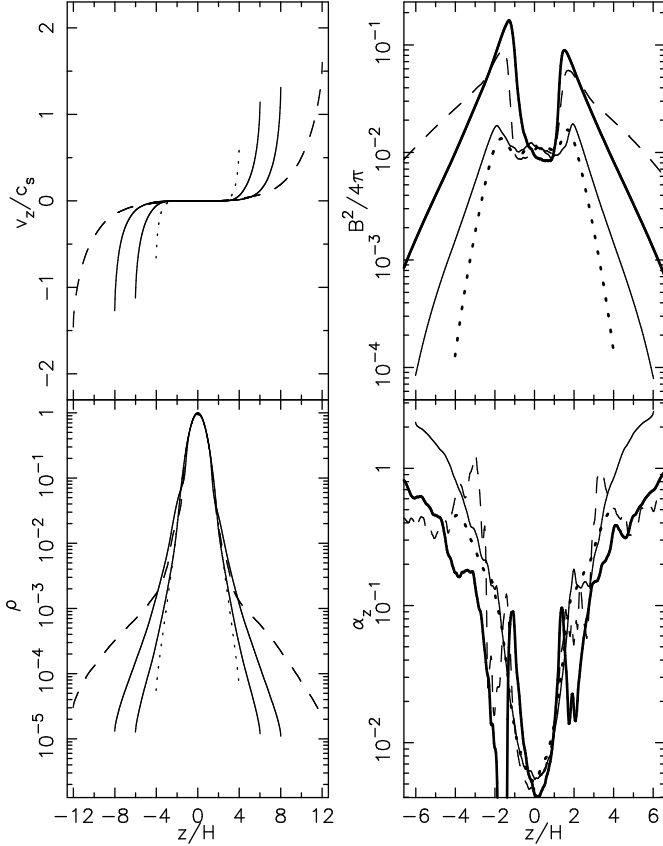


FIG. 16.— Comparison of the disk wind structures with the different box sizes. On the left, we display the time-averages of vertical velocity and density. On the right we compare the time-averages of magnetic energies and α values only in the $-6H < z < 6H$ region. The solid lines are the results with $r = 20H$ and box sizes, $-6H < z < 6H$ (Model VI) and $-8H < z < 8H$ (Model VII). The dashed lines are the results with $r = 10H$ and box size, $-12H < z < 12H$ (Model VIII). The dotted lines are the results of the reference case (Model II; $r \rightarrow \infty$ and $-4H < z < 4H$). On the right we use the thick lines for Model VII.

that the onsets of the disk winds take place at higher altitudes in larger box cases; the results depend on the simulation box size. However, the mass flux of the disk winds (ρv_z) do not show a monotonic behavior as presented in the bottom panel of Figure 17. By increasing the box size from $\pm 4H$ to $\pm 6H$, the mass flux decreases at first⁷. However, increasing the box size from $\pm 6H$ to $\pm 8H$, the mass flux increases slightly. The largest box size case with the smaller gravity, $r = 10H$, shows larger mass flux than these smaller box cases. The mass flux of the disk winds is bound by a lower limit and does not become further smaller even though we use a larger vertical box.

The dependence of the mass flux on the simulation box size can be explained by the saturation of the amplified magnetic fields (the top right panel of Figure 16). When we increase the box size from $\pm 4H$ to $\pm 6H$, the escaping mass from the disk surfaces becomes smaller at first. Accordingly, the escaping magnetic flux of the toroidal (y) and radial (x) components decrease, because

⁷ Although we do not take into account r in the case with the vertical box of $-4H < z < 4H$, this effect is negligible for sufficiently small z .

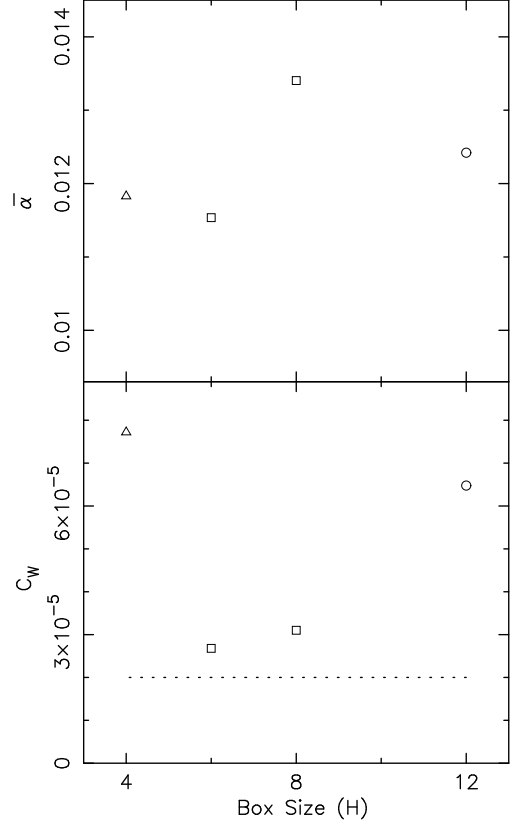


FIG. 17.— The $\bar{\alpha}$ values (top) and the mass flux of the disk winds (bottom) for the different sizes of the vertical simulation boxes. The triangles are the results of Model II ($r \rightarrow \infty$), the squares are the results with $r = 20H$ (Models VI & VII), and the circles are the results with $r = 10H$ (Model VIII). The dotted line is the level of $C_{w,\text{fl}}$.

the magnetic fields are frozen in the gas. The amplification of magnetic fields is balanced with the escape with the disk winds in addition to magnetic reconnections. In the larger box cases the escaping flux becomes smaller and the saturated level of magnetic fields increases. As a result of the larger magnetic pressure, the mass is lift up to higher locations (the bottom left panel of Figure 16). The increase of the density inhibits further decrease of the mass flux of the disk winds, ρv_z , in a self-regulated manner.

In spite of the increase of the magnetic field strength for larger boxes, α_z does not increase so much (the lower right panel of Figure 16). This is because the magnetic field of the large box cases around $z \approx 1.5H$ (the locations of the peaks) is dominated by the coherent toroidal component which does not contribute to the anisotropic Maxwell stress. Therefore, the integrated $\bar{\alpha}$ ($= \int dz \rho \alpha_z / \int dz \rho$), which directly determines the global mass accretion rate, does not depend on the vertical box size (the top panel of Figure 17).

The top left panel of Figure 16 shows that the average velocities of the disk winds do not still reach the escape speeds ($= \sqrt{2}r\Omega = \sqrt{2}(\frac{r}{H})H\Omega = 2(\frac{r}{H})c_s$). However, our conservative choice of the floor values, $C_{w,\text{fl}}$, probably gives a reasonable estimate (the dotted line of Figure 17), first because the mass flux seems bounded by the lower limit as explained above, and second because there are a

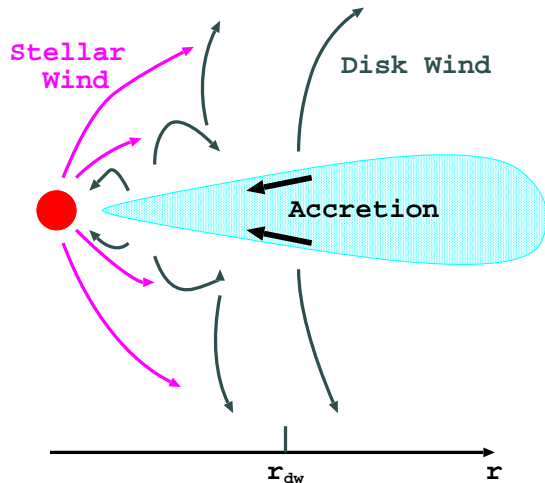


FIG. 18.— Schematic picture of dispersal of a protoplanetary disk by disk winds. The wind material in the outer region, $r > r_{\text{dw}}$, can stream out solely by the gravitational energy by accretion. On the other hand, the wind material in the inner location cannot escape by itself from the gravity of a central star. A fraction of the winds directly accrete to the central star after lift up. A fraction of the disk winds may be accelerated by the dynamical pressure of the stellar winds. If the stellar wind flux is not strong enough, the disk wind material returns back to the disk after transported outward. couple of mechanisms that favor the escape of the disk winds but are not included in this paper (see below).

5.4.2. Magnetocentrifugal Winds

Our local simulations do not take into account the acceleration (momentum input) of the disk winds by centrifugal force with global magnetic fields. If poloidal ($r - z$ components) magnetic field lines sufficiently incline with respect to an accretion disk, the gas can flow out along with the field lines by the centrifugal force (Blandford & Payne 1982; Kudoh & Shibata 1998). Such global magnetic fields will be common in protoplanetary disks as a result of the contraction of cold molecular clouds with interstellar magnetic fields. Therefore, our local simulations probably underestimate the momentum input to the disk winds.

5.4.3. Stellar Winds

So far, we have focused on the disk winds driven by MHD turbulence. Central T Tauri stars are also expected to drive stellar winds by the mass accretion from disks (Hirose et al. 1997; Matt & Pudritz 2005) and the surface convections (Cranmer 2008). Observations of T Tauri stars show that the outflow rates range from 10^{-11} to $10^{-8} M_{\odot} \text{ yr}^{-1}$, which is typically 0.01 - 1 times of the mass accretion rates (White & Hillenbrand 2004). Although it is difficult to determine the exact launching locations of the observed outflows, some fractions are expected to come from central stars (Edwards et al. 2006).

At present the stellar wind is regarded to give a minor effect to the dispersal of the gas component of protoplanetary disks (e.g. Shu, Johnstone, & Hollenbach 1992) because the stellar winds almost slide along the disk surfaces (Matsuyama, Johnstone, & Hollenbach 2009). However, if disk materials are lifted up as we have shown so far, the ram pressure of stellar winds can directly push away the lifted up materials because of the large elevation angle.

We discuss the role of stellar winds from a simple momentum balance. Let us consider a situation, in which the lifted up gas by disk winds floats above a disk and the radial stellar winds hit the floating gas. If we assume that both lifted up gas and stellar wind gas move together radially outward after the hitting, we can estimate the radial velocity of the moving gas, v_{cmb} , from the momentum balance as

$$(\dot{M}_{z,\text{in}} + W\dot{M}_{\star})v_{\text{cmb}} = W\dot{M}_{\star}v_{\star}, \quad (29)$$

where $\dot{M}_{z,\text{in}}$ is the rate of the mass that is supplied from disk winds but float above a disk without sufficient energy, W is the fraction of the solid angle obscured by the lifted up gas by the disk winds, and \dot{M}_{\star} and v_{\star} ($\approx 200 - 400 \text{ km s}^{-1}$) are the mass loss rate and velocity of the stellar winds. As a typical example, we consider the result of Model II at $t = 10^6 \text{ yr}$ (Figure 14). Then, $\dot{M}_{z,\text{in}} = 1.1 \times 10^{-9} M_{\odot} \text{ yr}^{-1}$; we assume the lifted up gas fill up to the height of $r/2$, which gives $W = \int_{\pi/2}^{\cot^{-1}(1/2)} d\cos\theta \approx 0.45$. The gas that is lifted up by the disk winds but does not have the sufficient energy will distribute in $r < r_{\text{dw}} (= 1.4 \text{ AU})$. Here, we compare v_{cmb} with the escape velocity at 1 AU, $v_{\text{esc},0} \approx 42 \text{ km s}^{-1}$ as a typical condition. Substituting these values into Equation (29), if $\dot{M}_{\star} > 4 \times 10^{-10} M_{\odot} \text{ yr}^{-1}$, $v_{\text{cmb}} > v_{\text{esc},0}$ is satisfied and the lifted up material can be blown away by the stellar winds.

If \dot{M}_{\star} is smaller than this value, the stellar winds can blow away the disk wind material at sufficiently high altitudes where the density is low. The disk wind material at lower heights will move outward after hit by the stellar winds but again return back to the disk without sufficient energy. When the returning location becomes $r > r_{\text{dw}}$, the gas finally flow out by the disk winds. (see Figure 18 for the schematic picture).

6. SUMMARY

In this paper, we have shown that the MRI-driven protoplanetary disk winds disperse the gas component of disks from the inside out. If net vertical magnetic fields with moderate strength exist, the disk winds and accretion switch-on from the inner locations, which forms an expanding inner hole. This mechanism naturally explains observed transitional disks with inner holes. Model calculations that incorporate UV or X-ray photoevaporation with accretion also expects an inner hole at the later stage after the significant fraction of the gas disappears (Alexander, Clarke, & Pringle 2006; Gorti, Dullemond, & Hollenbach 2009). The main difference of our mechanism from the photoevaporation processes is that the MRI-driven disk winds expect an inner hole from the early times and its size gradually grows from $< 0.1 \text{ AU}$ to several tens AU during the evolution of $\sim 10^7$ years.

Future high resolution observations by ALMA will be able to resolve inner holes with \sim a few AU at distance of 100 pc. We hope that observations of protoplanetary disks with various epochs will reveal the time-evolution of inner holes.

The dead zone does not affect the disk winds so much and the effect is only limited at the early epoch ($\lesssim 10^6$ years) of the disk evolution, because the MRI-driven disk winds are driven from the surface regions with sufficient ionization degree. Even though a large dead zone forms around the midplane, the disk winds are also driven intermittently with quasi-periodic cycles of 5-10 rotations as a result of the breakups of large-scale channel flows, similarly to the no dead zone simulation (SI09). The intermittency of the simulated disk winds should be observed as the variation of the disk surfaces, which might explain the observed large time variations of young stars (Wisniewski et al. 2009; Muzerolle et al. 2009; Bary, Leisenring, & Skruskie 2009).

The inside-out clearing of protoplanetary disks by the MRI-driven disk winds suppress the infall of boulders because the outward force by gas pressure gradient is small. This is suitable condition for the formation of planetesimals by aggregation, where we also need to examine sticking condition to study the actual growth of solid

materials (e.g. Okuzumi 2009). The inside-out clearing may also increase the dust-to-gas ratio in the inner part of a disk, which is also favorable for the formation of planetesimals by gravitational instability (Sekiya 1998; Youdin & Shu 2002; Johansen et al. 2007). The migration of planets is also suppressed in the inner region where the gas is dispersed at early times. Then, the inward migration of newly formed (proto-)planets stop at a certain location as shown in Figure 12. On the other hand, the gas remains in the outer region, so that the formation of gas planets can proceed there.

The authors thank an anonymous referee for many valuable comments. This work was supported in part by Grants-in-Aid for Scientific Research from the MEXT of Japan (TKS: 19015004, 20740100, and 22864006 SI: 15740118, 16077202, and 18540238), and Inamori Foundation (TKS). Numerical computations were in part performed on Cray XT4 at Center for Computational Astrophysics, CfCA, of National Astronomical Observatory of Japan.

REFERENCES

- Alexander, R. D., Clarke, C. J. Pringle, J. E. 2006, MNRAS, 369, 229
- Balbus, S. A. & Hawley, J. F. 1991, ApJ, 376, 214
- Balbus, S. A. & Hawley, J. F. 1998, Rev. Mod. Phys., 70, 1
- Bary, J. S., Leisenring, M., & Skruskie, M. F. 2009, ApJ, in press (arxiv:0910.3454)
- Blaes, O. M., Balbus, S. A., ApJ, 421, 163
- Blandford, R. D. & Payne, D. G. 1982, MNRAS, 199, 883
- Brandenburg, A., Nordlund, \varnothing A., Stein, R., F., & Torkelsson, U. 1995, ApJ, 446, 741
- Calvet, N. et al. 2005, ApJ, 630, L185
- Chiang, E. & Murray-Clay, R., 2007, Nature Phys., 3, 604
- Cranmer, S. R. 2008, ApJ, 689, 316
- Davis, S. W., Stone, J. M., & Pessah, M., E. 2010, ApJ, 713, 52
- Edwards, S., Fischer, W., Hillenbrand, L. A., & Kwan, J. 2006, ApJ, 646, 319
- Ercolano, B., Clarke, C. J., & Drake, J. J. 2009, ApJ, 699, 1639
- Espaillet, C. et al. 2008, ApJ, 689, L145
- Fromang, S., Terquem, C. & Balbus, S. A. 2002, MNRAS, 329, 18
- Gammie, C. F. 1996, ApJ, 457, 355
- Ghosh, P. & Lamb, F. K. 1979, ApJ, 232, 259
- Glassgold, A. E., Najita, J. & Igea, J. 1997, ApJ, 480, 344
- Gorti, U., Dullemond, C. P., & Hollenbach, D. 2009, ApJ, 705, 1237
- Gressel, O. 2010, MNRAS, in press
- Haisch, K. E., Jr., Lada, E. A., & Lada, C. A. 2001, ApJ553, L153
- Hayashi, C. Prog. Theoretical Phys. Supp., 70, 35
- Hawley, J. F., Gammie, C. F., & Balbus, S. A. 1995, ApJ, 440, 742 -
- Hernández, J., Hartmann, L., Calvet, N., Jeffries, R. D., Gutermuth, R., Muzerolle, J., & Stauffer, J. 2008, ApJ, 686, 1195
- Hirose, S., Uchida, Y., Shibata, K., & Matsumoto, R. 1997, PASJ, 49, 193
- Hughes, A. M. et al. 2009, ApJ698, 131
- Ida, S., & Lin, D. N. C. 2004, ApJ, 604, 388
- Ilgner, M. & Nelson, R. P. 2006, A&A, 445, 205
- Inutsuka, S. & Sano, T. 2005, ApJ, 628, L155
- Johansen, A., Oishi, J. S., Low, M.-M. M., Klahr, H., Henning, T., & Youdin, A. 2007, Nature, 448, 1022
- Kato, M. T., Nakamura, K. Tandokoro, R., Fujimoto, M. & Ida, S. 2009, ApJ, 691, 1697
- Kenyon, S. J. Yi, I. & Hartmann, L. 1996, ApJ, 462, 439
- Kudoh, T. & Shibata, K. 1998, ApJ, 508, 186
- Latter, H. N., Fromang, S. & Gressel, O. 2010, MNRAS in press (arxiv:1004.0109)
- Lynden-Dell, D. & Pringle, J. E. 1974, MNRAS, 168, 603
- Machida, M., Hayashi, M. R., & Matsumoto, R. 2000, ApJ, 532, L67
- Matsumoto, R. & Tajima, T. 1995, ApJ, 445, 767
- Matsumura, S., Pudritz, R. E., & Thommes, E. W. 2007, ApJ, 1609
- Matsuyama, I., Johnstone, D., & Hartmann, L. ApJ, 582, 893
- Matsuyama, I., Johnstone, D., & Hollenbach, D. 2009, ApJ, 700, 10
- Matt, S. & Pudritz, R. E. 2005, ApJ, 632, L135
- Michikoshi, S. & Inutsuka, S.-I. 2006, ApJ, 641, 1131
- Miller, K. A. & Stone, J. M. 2000, ApJ, 534, 398
- Muzerolle, J. et al. 2009, ApJ, 704, L15
- Nishikori, H., Machida, M., & Matsumoto, R. 2006, ApJ, 641, 862
- Okuzumi, S. 2009, ApJ, 698, 1122
- Owen, J. E., Ercolano, B., Clarke, C., & Alexander, R. D. 2010, MNRAS, 401, 1415
- Parker, E. N. 1955, ApJ, 122, 293
- Parker, E. N. 1966, ApJ, 145, 811
- Pessah, M. E., Chan, C.-K., & Psaltis, D. 2007, ApJ, 668, L51
- Pringle, J. E. 1981, ARA&A, 19, 137
- Sano, T., Miyama, S. M., Umebayashi, T., & Nakano, T. 2000, ApJ, 543, 486
- Sano, T., Inutsuka, S., Turner, N. J., & Stone, J. M. 2004, ApJ, 605, 321
- Sekiya, M. 1998, Icarus, 133, 298
- Shakura, N. I. & Sunyaev, R. A. 1973, A&A, 24, 337
- Shi, J., Krolik, H., & Hirose, S. 2010, ApJ, 708, 1716
- Shu, F. H., Johnstone, D., & Hollenbach, D. 1992, Icarus, 106, 92
- Suzuki, T. K. & Inutsuka, S. 2009, ApJ, 691, L49 (SI09)
- Tanaka, H., Takeuchi, T. & Ward, W. R. 2002, ApJ, 565, 1257
- Takeuchi, T., Clarke, C. J., & Lin, D. N. C. 2005, ApJ, 627, 286
- Telleschi, A., Güdel, M., Briggs, K. R., Audard, M., & Palla, F. 2007, A&A, 468, 425
- Turner, N. J., Sano, T., & Dziourkevitch, N. 2007, ApJ, 659, 729
- Umebayashi, T. & Nakano, T. 1980, PASJ, 32, 405
- Vishniac, E. & Brandenburg, A. 1997, ApJ, 475, 263
- Ward, W. R. 1977, ICARUS, 126, 261
- Weidenschilling, S. J. 1977, MNRAS, 180, 57
- White, R. J. & Hillenbrand, L. A. 2004, ApJ, 616, 998
- Wisniewski, J. P. et al. 2009, ApJ, 682, 548
- Yoshimura, H. 1975, ApJ, 201, 740
- Youdin, A. N. & Shu, F. H. 2002, ApJ, 580, 494